공학박사학위논문

유효 임피던스 제어 탄성 메타물질을 이용한 전방향 전단 수평파 출력 증폭

Effective Impedance-Controlled Elastic Metamaterials for Emission Enhancement of Omnidirectional Shear-Horizontal Waves

2023년 8월

서울대학교 대학원

기계항공공학부

김 홍 재

유효 임피던스 제어 탄성 메타물질을 이용한 전방향 전단 수평파 출력 증폭

Effective Impedance-Controlled Elastic Metamaterials for Emission Enhancement of Omnidirectional Shear-Horizontal Waves

지도교수 김 윤 영

이 논문을 공학박사 학위논문으로 제출함

2023년 4월

서울대학교 대학원

기계항공공학부

김 홍 재

김홍재의 공학박사 학위논문을 인준함

2023년 6월

위 원 장 : 김 도 년

부위원장 : 김 윤 영

위 원 : 양 진 규

위 원 : 오 주 환

위 원 : 이 혁

ABSTRACT

Effective Impedance-Controlled Elastic Metamaterials for Emission Enhancement of Omnidirectional Shear-Horizontal Waves

Hong Jae Kim
Department of Mechanical and Aerospace Engineering
The Graduate School
Seoul National University

This dissertation aims to investigate practical techniques to significantly enhance the emission of omnidirectional shear horizontal wave sources, and to provide background physics and design methods for elastic metamaterials. Since the intensity of ultrasonic wave is directly related to the inspection accuracy, various approaches have been studied to improve the performance of ultrasonic wave transducers. In particular, the intensity of an omnidirectional ultrasonic transducer that can effectively respond to a wide inspection range decreases in the propagation direction due to its unique physical features, further raising the necessity. Additionally, while the shear horizontal wave mode has its advantages, it is challenging to secure high intensity. However, existing studies have been developed limited to the internal design of ultrasonic wave transducers, so the expected

intensity is limited considering a practical application.

This study proposes a non-destructive method to attach a metamaterial to the inspection object around the transducer to significantly enhance the emission of ultrasonic waves regardless of the transducer's internal design.

First, the metamaterial ring is designed as a resonator of segmented mass and springs to cause two physical principles: 1) low impedance environment and 2) Fabry-Perot resonance phenomenon. By interpreting the mechanical mechanism of the metamaterial ring and the equivalent system homogenized with an effective medium, we explain the emission enhancement of ultrasonic waves. The transducer generates ultrasonic waves with larger output in a low impedance environment and overcomes the low transmission problem due to the impedance difference generated at the boundary through the Fabry-Perot resonance phenomenon. On the other hand, when performing a non-destructive test, it is necessary to consider the sensitivity of the metamaterial to the input cycles in that a short period of signal is preferred for inspection accuracy. In response, this study proposes a metamaterial superstrate capable of increasing the impedance of the local area. The physical phenomenon is identified using the newly defined transfer matrix and scattering matrix, and the necessary properties are investigated. The superstrate causes partial reflection and transmission of ultrasonic waves by generating impedance differences, which significantly enhance the wave emission by only the ratio of impedance differences under the geometric conditions forming the Fabry-Perot cavity. In addition, the superstrate structure, designed as a non-resonance type, is relatively insensitive to

the number of cycles, so it is very practical. The proposed elastic metamaterials are expected to have high potential to the field of non-destructive testing using ultrasonic waves that require power enhancement.

Keywords: Elastic metamaterial, Emission enhancement, Omnidirectional shear horizontal wave, Effective impedance, Fabry-Perot cavity

Student Number: 2016-25899

CONTENTS

ABSTRACT ..... **i**

CONTENTS ..... **iv**

LIST OF TABLES ..... **vii**

LIST OF FIGURES ..... **viii**

CHAPTER 1. INTRODUCTION **1**

1.1 Motivation 1

1.2 Research objectives 3

1.3 Outline of thesis 4

CHAPTER 2. Theoretical Background **7**

2.1 Overview 7

2.2 Waves in a cylindrical coordinates 8

2.2.1 Wave equation and motion 8

2.2.2 Simplified model of the transducer system 10

2.3 Wave propagation in matrix form 11

CHAPTER 3. Meta-ring for enhancing emission efficiency of omnidirectional SH waves **14**

3.1 Overview 14

3.2 Analysis of the physics in the meta-ring 19

3.2.1 Wavefield equation of the transducer system with the meta-ring 20

3.2.2 Wavefield equation of the equivalent system 25

3.3 Design of meta-ring with analytic and FEM simulation 32

3.3.1 Analysis results of the transduction efficiency enhancement using the meta-ring 33

3.3.2 Effects of meta-ring location and resonance frequency 35

3.3.3 Finite element analysis to design the meta-ring structure 37

3.3.4 Numerical simulations for transduction efficiency enhancement by meta-ring 39

3.3.5 Numerical simulations to investigate effects of input signal cycles 41

3.4 Experimental validation 42

3.5 Summary 44

CHAPTER 4. High gain elastic metamaterial superstrate for omnidirectional SH wave emission 58

4.1 Overview 58

4.2 Theoretical analysis 63

4.2.1 Transfer matrix and scattering parameter with the effective medium 64

4.2.2 Gain of emission enhancement by effective medium layer.....67

4.3 Design of the elastic metamaterial superstrate 74

4.3.1 Characteristics of elastic metamaterial superstrate.....75

4.3.2 Analytic discussion of elastic metamaterial superstrate 76

4.4 Numerical simulation of the emission enhancement.....78

4.4.1 Harmonic analysis 79

4.4.2 Transient analysis 81

4.5 Experimental validation 82

4.6 Summary 84

CHAPTER 5. Conclusions 97

APPENDIX A. Validation of approximation in theoretical analysis 101

A.1 Background for far-field approximation for meta-ring 101

A.2 Validation of transfer matrix and scattering matrix approximation 102

REFERENCES 107

ABSTRACT (KOREAN) 117

ACKNOEWLEDGEMENTS 120

LIST OF TABLES

Table 3.1 Peak frequency and gain results of the theoretical model/FEM/FEM+bonding simulation and experiment. 46

Table 4.1 The geometric design solutions of the variable W at the target frequency 70 kHz. (unit: mm) 86

Table 4.2 The geometric design solutions of the variable d at the target frequency 70 kHz. (unit: mm) 87

LIST OF FIGURES

Fig. 2.1 Cylindrical coordinate system used for the analysis of the omnidirectional shear horizontal wave physics. 13

Fig. 3.1 Schematics of the meta-ring model with OSH-MPTs. (a) Illustrations of an actuated wave signal generated by a transducer decreasing inverse squarely due to omnidirectionality and (b) a boosted wave signal when a meta-ring is attached. ... 47

Fig. 3.2 (a) Proposed theoretical model for the meta-ring with a transducer. The detailed geometric dimensions of the meta-ring structure in the T-shaped beam are s_x = 2 mm, s_y = 3 mm, m_x = 6 mm, m_y = 3 mm, and the test plate thickness p_t = 1 mm. (b) One-dimensional model depicting the axisymmetric plate as a bar and the meta-ring as a mass-spring resonator. (c) A homogenized equivalent model with the mechanical effects of the meta-ring smeared in the bar where the zone affected by the meta-ring is assumed to have an effective impedance Z_{eff}. The symbol $\widetilde{F}_{trd}$ represents the resultant pin-forces generated by the magnetostrictive patch. 48

Fig. 3.3 Analytic solutions of the SH wave in a bar with a mass-spring model as a function of frequency. (a) Radiated displacement field $|u_\theta|$ of the nominal and meta-ring attached cases. (b) Enhancement gain function $|H(\omega)|$ of the meta-ring. (c) Magnitude and (d) phase of the reflection coefficient at the boundary of the mass-spring model. 49

Fig. 3.4 Analytic solutions of the SH wave in an equivalent bar system as a function

of frequency. (a) Ratio of effective impedance to nominal impedance Z_{eff}/Z_0 through the retrieval and asymptotic solution and (b) effective distance W_{eff}. (c) The explicit enhancement gain function $|H(\omega)|$ with an asymptotic dotted line of the inverse square root of the impedance ratio. 50

Fig. 3.5 (a) Contours of the enhancement gain $|H(\omega,W)|$ as functions of the frequency *f* and distance *W* under fixed geometries of the T-shaped cross-section of the meta-ring. (b) $|H(\omega)|$ as a function of frequency *f* along the equi-*W* lines for *W* = 48 mm, 52 mm, and 56 mm. (c) Gain and full width at half maximum along the distance *W* of the meta-ring. (d) Variation of the normalized target frequency along the distance *W*. 51

Fig. 3.6 Finite element analysis to extract mass *m* and stiffness *s* of the meta-ring structure. (a) SH eigenmode of the meta-ring fragment and (b) varying eigenfrequency of the structure along the change in variable *W*. (c) Angular deformed shape of the meta-ring fragment under an applied force (f_n) perpendicular to the cross-section and (d) the varying stiffness of the structure along the change in the distance variable *W*. 52

Fig. 3.7 (a) Finite element model for verifying an effect of the meta-ring structure under harmonic conditions. (b) Parametric sweep analysis on variables *W* and frequency *f* to find a boosting phenomenon. (c) Comparison of the theoretical/FEM simulation results of the enhancement gain function $|H(\omega)|$ using the meta-ring. (d) Normalized von-mises stress fields in the FEM simulation results for the

conventional transducer system and the transducer boosted with the meta-ring at a peak frequency of 68.7 kHz. 53

Fig. 3.8 The output shear horizontal displacement signals are predicted by the transient analysis. The considered input signals are (a) the Hanning-windowed 10-cycle sine wave, (b) 30-cycle sine wave, (c) 50-cycle sine wave, and 100-cycle sine wave. 54

Fig. 3.9 Snapshots from animated images of the transient analysis using 100-cycle sine wave inputs. 55

Fig. 3.10 The output displacement signals corresponding to the SH and the Lamb waves (corresponding to the out-of-plane displacement) are calculated by the finite element analysis 56

Fig. 3.11 Experimental demonstration in a thin plate. (a) Setup for experiments with a prototype of the meta-ring. A circular MPT is used to ensure the actuating and sensing of an omnidirectional SH wave. (b) A comparison of the FEM simulation considering the epoxy resin bonding layer (DP100, layer thickness = 0.2 mm) and experiment results for the enhancement gain $|H(\omega)|$ as a function of the frequency that denote the effect of the meta-ring on the radiated strain field $|S|$ 57

Fig. 4.1 Schematics of an elastic metamaterial superstrate enhancing an omnidirectional shear horizontal wave emission. (a) Propagation pattern of the waves generated from an excitation source on a thin plate structure. The amplitude of the wave expressed by the darkness of the color is decreased with the inverse

square of the propagation distance. (b) Illustrations of an emission enhancement through the installation of the superstrate structure. 88

Fig. 4.2 Analytical model of (a) single layer and (b) multiple layers of an effective medium substituting an elastic metamaterial superstrates in an axis-symmetric one-dimensional propagation problem. 89

Fig. 4.3 (a) The phase velocity plot of the shear horizontal wave modes and the target frequency range interest. (b) Analytic concept of an effective medium consists of the geometric parameters W and d , and (c) realized structure of the elastic metamaterial superstrate design with the same geometric parameters and the newly added thickness variable t_s 90

Fig. 4.4 Analytic solution of an emission enhancement (gain) and two Fabry-Perot conditions of the geometric parameters W and d of effective medium.....91

Fig. 4.5 (a)Analytical gain as functions of the geometric design parameters W and d of the effective medium. The impedance ratio z_r of the effective medium to the normal medium is set to 3, and the effective wavenumber is the same as that of the normal medium. (b) Plot of analytical gain converted to sine fields for each geometric variable.....92

Fig. 4.6 Analytical model of (a) single layer and (b) multiple layers of an effective medium substituting an elastic metamaterial superstrates in an axis-symmetric one-dimensional propagation problem. 93

Fig. 4.7 Comparison the gain enhancement. Each results indicate FEM simulation of

elastic metamaterial superstrate design and the theory with an effective medium. Gain as a function of frequency is plotted under a following condition; (a) impedance ratio $z_r = 2$, (b) impedance ratio $z_r = 3$, and (d) impedance ratio $z_r = 4$. 94

Fig. 4.8 Gain dependence on the input signal cycles. Transient analysis results of the input signal of (a) 10-cycles sinusoid, and (b) 20-cycles sinusoid, and (c) 30-cycles sinusoid without and with the elastic metamaterial superstrate. 95

Fig. 4.9 The experimental setup and result data for validation. (a) Experimental setup with an illustration of the designed metamaterial superstrate installed on an aluminum plate around the transmitter. (b) The measured gain(squares) compared to that of theory(solid lines) and FEM(circles). 96

Fig. A.1 Background for far-field approximation for meta-ring. (a) Real and imaginary parts of the exact and asymptotic forms of 1st order Hankel function. (b) Real and imaginary parts of the exact and asymptotic forms of 2nd order Hankel function. (c) Error rates of the 1st and 2nd order Hankel functions in magnitude and phase.....104

Fig. A.2 Comparison of the exact and approximated forms of scattering matrix S. Green and brown curves denote component of exact form and approximated form, respectively.....105

Fig. A.3 Comparison of the exact and approximated forms of scattering matrix S. Green and brown curves denote component of exact form and approximated form, respectively.....106

CHAPTER 1.
INTRODUCTION

1.1 Motivation

As interest in non-destructive testing to investigate the safety and reliability of structures increases, the importance of ultrasound research used for non-destructive testing is being emphasized. Here, the chronic requirement is to generate high power ultrasound. The power of waves is a key problem that determines the accuracy of the inspection and the test performance, such as coverage, resolution, and power consumption dominantly. In addition, an omnidirectional transducer is used to effectively examine a large-scale test object, which requires higher power due to the problem of limited inspection range and performance due to the inherent physical features of reducing intensity through radiation. For this reason, numerous studies have been conducted on the development of ultrasonic transducers, and a variety of design principles and methods have been proposed. However, there is an obvious limitation in that the methods are exclusive to each form of transducer or increase the complexity of the design. To address this problem, one aims to provide a practical

alternative approach to overcome the low power problem of the ultrasonic transducer through impedance modulation and conforming a Fabry-Perot resonance cavity utilizing the concept of metamaterials.

Recently, metamaterials have been investigated for various purposes, as their artificially designed structures enable attaining unfeasible physical properties and wave manipulation with existing materials. In general, metamaterial structures designed in a two-dimensional plane have attracted the most attention, and designs based on phononic crystals or resonance structures have been mainly discussed. However, this strategy is unsuitable for a practical application, non-destructive testing, because it requires destructive processing into the object. In contrast, metamaterials, such as pillars, auxetic, kirigami, resonator, and superstrate structures, designed in out-of-plane design spaces, have a high possibility of practical usefulness. These metamaterial design methods have mainly responded to unidirectional propagation problems, and no research has yet been conducted on methodologies that can implement wave emission enhancements or directly change impedance in omnidirectional problem conditions.

In this work, one proposes a novel metamaterial that can highly enhance the emission of omnidirectional shear horizontal waves by attaching a simple, transducer-independent structure to the object. The function of each metamaterial is to modulate impedance, which is a representative physical property considered in the elastic domain. By controlling the impedance of a specific region, the amplitude of the wave generated by transducer is increased, but so does the impedance mismatch. However,

When the newly revealed special Fabry-Perot resonance conditions for omnidirectional waves are satisfied, metamaterial may form a Fabry-Perot resonance cavity inside, and a high gain of enhanced emission of radio sources can be expected.

1.2 Research objectives

This work aims to enhance the emission of omnidirectional shear horizontal waves, and ultimately presents practical techniques to improve the performance of various ultrasonic applications, including nondestructive testing and structural health monitoring. Despite the practical usefulness of omnidirectional propagation waves, the development of various types of elastic metamaterials has been studied focusing on unidirectional propagation wave problems because the physical interpretation of omnidirectional propagation waves expressed in complex forms such as Bessel functions is difficult. Throughout this thesis, one dedicated to establish the solid theoretical analysis and find out the clear design methodologies of high gain elastic metamaterials.

In this dissertation, two types of elastic metamaterials designed with different physical interpretations are suggested. One is a metamaterial ring based on the resonator structure designed on a subwavelength scale, which lowers the effective impedance of the surrounding area and enhances wave emission at the Fabry-Perot resonance frequency. To comprehend the wave phenomena, two analytical models:

1) mechanical behavior of structures segmented by mass and rigidity, and 2) equivalent systems replaced by special effective medium are investigated. The design of metamaterials is determined by two design variables matching to a theoretical model. The realized resonator structure, indeed, enhance the wave emission. Next, an elastic metamaterial superstrate designed in a wavelength scale is developed to increase the local impedance and form a Fabry-Perot cavity inside, resulting in wave emission enhancement. In this part, a newly proposed theoretical model with an effective medium is analyzed and explicitly reveals the conditions for Fabry-Perot resonance and the achievable gain. Following the analysis, a non-resonant design of a structure with the required effective property value is devised, and the corresponding response is confirmed. Finally, the effectiveness and performance of each metamaterial are evaluated through transient analysis and experiments in order to assess their applicability.

1.3 Outline of thesis

The thesis is organized as follows.

In **<Chapter 2>**, the theoretical background of omnidirectional shear horizontal waves will be presented. First, to deal with omnidirectinality, the wave equation in cylindrical coordinates will be reviewed. The general forms of the displacement, strain, and stress fields in elastic media are described. Next, the analytic model of

wave actuation by omnidirectional transducers, regardless of types, such as MPT, EMAT, and PZT, will be discussed. In the last, we will suggest the description of the wave motion in a matrix form to effectively analyze the generalized wave emission enhancement theory related to the multiple overlapping of the metamaterials arrangements.

In **<Chapter 3>**, the metamaterial ring of resonance structures that achieve wave emission enhancement is proposed. The metamaterial ring is installed around the wave source and modifies the wave actuation circumstance. We will explain the underlying physics with the two different approaches. First, we investigate the theoretical system with a discrete mass-spring model. The mechanical behavior of the meta-ring and the resultant emission modification will be analyzed. Next, we reveal the physical implications of the meta-ring through the equivalent system substituted with the effective medium. We elucidate the impedance and Fabry-Perot resonance conditions for achieving the high gain emission enhancement of the waves.

In **<Chapter 4>**, the non-resonance structure, elastic metamaterial superstrate, is suggested. Superstrate has a simple structure that can freely determine the thickness of the circular ring shape, which can be installed around the wave source to amplify the emission greatly. At first, we newly define the transfer matrix and scattering matrix method interpreting the wave emission enhancement phenomenon with the existence of an effective medium. Based on the physical foundation, the superstrate

structure realizing desired mechanical properties is determined by using the unique nondispersive characteristics of the fundamental shear horizontal wave mode. The designed superstrate structure carries out the modulation of the physical features that locally increase the effective impedance and result in a Fabry-Perot cavity inside. Also, its high performance for short periods of input signals, which is an important factor in practical application, is confirmed. Furthermore, through the proposed theoretical analysis, we demonstrate the effectiveness of multiple emission enhancement via the arrangement of superstrates.

In **<Chapter 5>**, the conclusion of the thesis will be presented..

CHAPTER 2.
Theoretical Background

2.1 Overview

In this chapter, we will review the theoretical background for wave physics in the Cylindrical coordinate system, which differs from that in the Cartesian coordinate system. Since the purpose of this study is to improve the output of omnidirectional propagation shear horizontal waves, we will cover the theoretical introduction to analyzing the wave systems shown in Chapters 3 and 4. First, we introduce the wave equation and motion of the omnidirectional shear horizontal waves in the Cylindrical coordinates. Using these wave descriptions, we can simplify the incident, reflected, and transmitted wave components in elastic media. Next, the theoretical model representing the actuating mechanism of the ultrasonic transducer system is considered. The simplified model is useful for analyzing the wave systems presented in Chapters 3 and 4. In the final section, 2.3, the matrix form of wave propagation is reviewed. The matrix form is an efficient tool that can explicitly denote incident and reflected components in each medium and easily calculate reflection, transmission,

and even system gain obtained by the proposed elastic metamaterials. Also, the defined matrix form in section 2.3 will facilitate analyzing the generalized Fabry-Perot cavity model with multiple arrangements of the effective medium.

2.2 Waves in a cylindrical coordinates

Before we understand the principles of elastic metamaterials that enhance the emission of omnidirectional propagation shear horizontal waves and discuss design methods, we must first understand the fundamental physics of omnidirectional propagation waves defined in the cylindrical coordinates system. In this section, we will investigate the basic wave equation and the shear horizontal wave motion to be utilized in the Chapter 3 and 4. Also, we address the actuation modeling of the transducer and regard the magnitude of the excitation wave at each frequency as a constant.

2.2.1 Wave equation and motion

To describe the shear wave motion in a transducer system in Fig. 2.1, the wave equation is written in terms of the vector potential ψ denoted as

$$\nabla^2 \psi = \frac{1}{c_s^2} \frac{\partial \psi}{\partial t^2} \tag{2.1}$$

where c_s denote the phase velocity of the shear wave in the elastic medium and t is time. Considering the lowest shear horizontal mode with an omnidirectional propagation condition $(\partial / \partial \theta = 0)$, the displacement component u_θ in a cylindrical coordinate system (r, θ, z) is given by

$$\psi = \psi_z \widehat{e_z} \tag{2.2}$$

where ψ_z is the only potential considered in this problem. Then, substituting Eq. (2.2) into Eq. (2.1), the former becomes in the form of Bessel's differential equation:

$$\nabla^2 \psi_z - \frac{1}{c_s^2}\frac{\partial \psi_z}{\partial t^2} = \frac{\partial^2 u_\theta}{\partial r^2} + \frac{1}{r}\frac{\partial u_\theta}{\partial r} + \left(\frac{\omega^2}{c_s^2} - \frac{1}{r^2}\right) u_\theta = 0 \tag{2.3}$$

under the time-harmonic condition $e^{i\omega t}$ (ω : angular frequency, $i = \sqrt{-1}$), which is omitted throughout the analysis. Therefore, the solution to the displacement u_θ can be expressed as

$$u_\theta(r) = AkH_1^{(1)}(kr) + BkH_1^{(2)}(kr) \tag{2.4}$$

and the strain is expressed as

$$\gamma_{r\theta} = \frac{\partial u_\theta}{\partial r} - \frac{u_\theta}{r} = -Ak^2 H_2^{(1)}(kr) - Bk^2 H_2^{(2)}(kr) \tag{2.5}$$

where k denotes the wavenumber. Here, $H_\nu^{(1)}$ and $H_\nu^{(2)}$ represent the Hankel functions of the first and second kind in order of ν. In addition, coefficients A and B denote the amplitudes of the outward and inward propagating waves, respectively.

2.2.2 Simplified model of the transducer system

Fig. 2(a) shows the schematics of the entire system of an omnidirectional SH0 wave-generating magnetostrictive patch transducer with a meta-ring configured in a T-shaped beam installed on a thin plate. It should be noted that the beam consisting of the mass and spring parts functions as an axisymmetric resonator designed only to couple with the omnidirectional propagating shear horizontal wave motion. In fact, the only wave propagating in the plate is the lowest mode of the in-plane shear horizontal wave (SH0) in the frequency of interest. All structures, including the OSH-MPT, are axisymmetric along the center, and therefore, the wave motion in the plate described in cylindrical coordinates can be modeled as a one-dimensional bar, as depicted in Fig. 2(b). As employed in earlier studies [18], the wave generation mechanism of MPT is explained using the pin-end-force model. With an assumption that the annular magnetostrictive patch is bonded perfectly onto a plate, the generation of the shear strain $\gamma_{r\theta}(r)$ induced by the tractions at the boundary of the patch with a size of inner radius a_1 = 15 mm and outer radius a_2 = 20 mm can be expressed as (shown in Appendix A):

$$\gamma_{r\theta,i}(r) = c\tau_{a_i} k^2 H_1^{(1)}(kr), \quad i = 1, 2 \tag{2.6}$$

where k is the wavenumber, τ_{a_i} (i = 1, 2) is the coefficient to denote the magnitude of the tractions, and c is a constant used to match the dimensions between the left and right sides of Eq. (2.6). By superposing the two separated displacement sources

of the patch in the opposite circumferential direction, the total wave source is modeled as follows:

$$\gamma_{r\theta,tot}(r)=\gamma_{r\theta,1}(r)-\gamma_{r\theta,2}(r)=c\left(\tau_{a_1}-\tau_{a_2}\right)k^2H_1^{(1)}(kr)\triangleq F_{trd}H_1^{(1)}(kr) \qquad (2.7)$$

The transducer-dependent magnitude F_{trd} is assumed to be given. Eq. (2.7) states that the actuation generated by the employed transducer configuration can be assumed as a single concentrated source.

2.3 Wave propagation in matrix form

In a radial one-dimensional propagation problem with axis-symmetry, we can represent the shear horizontal displacement fields u_θ using Eq. (2.4). With the coefficients of outward and inward going wave component and the wavenumber, respectively, A_{out}, B_{in} and k, the stress fields can also be calculated as follow

$$\sigma_{r\theta}(r)=-A_{out}k\omega zH_2^{(1)}(kr)-B_{in}k\omega zH_2^{(2)}(kr) \qquad (2.8)$$

where ω denotes the angular frequency of the wave. Here, the parameter z denotes the impedance of the medium, and for the thin plate in a thickness p_t, we can describe the mechanical impedance z for the shear horizontal wave as a $p_t\sqrt{\rho G}$ (ρ : density, G : shear modulus). Combining Eqs. (2.4) and (2.8), the wave motion in a radial one-dimensional propagation in an elastic medium with the mechanical properties k and z is transformed to the matrix form of

$$\begin{bmatrix} u_\theta \\ \sigma_{r\theta} \end{bmatrix} = Z(k,z)H(k,r)\begin{bmatrix} A_{out} \\ B_{in} \end{bmatrix} \tag{2.9a}$$

Where

$$\begin{bmatrix} u_\theta \\ \sigma_{r\theta} \end{bmatrix} = Z(k,z)H(k,r)\begin{bmatrix} A_{out} \\ B_{in} \end{bmatrix} \tag{2.9b}$$

$$\begin{bmatrix} u_\theta \\ \sigma_{r\theta} \end{bmatrix} = Z(k,z)H(k,r)\begin{bmatrix} A_{out} \\ B_{in} \end{bmatrix} \tag{2.9c}$$

which is similar to the matrix form of a one-dimensional plane wave. By using Eqs. (2.9a-c), we are able to analyze the wave physics of omnidirectional shear horizontal wave propagation through the effective medium in the respect of the coefficient relation.

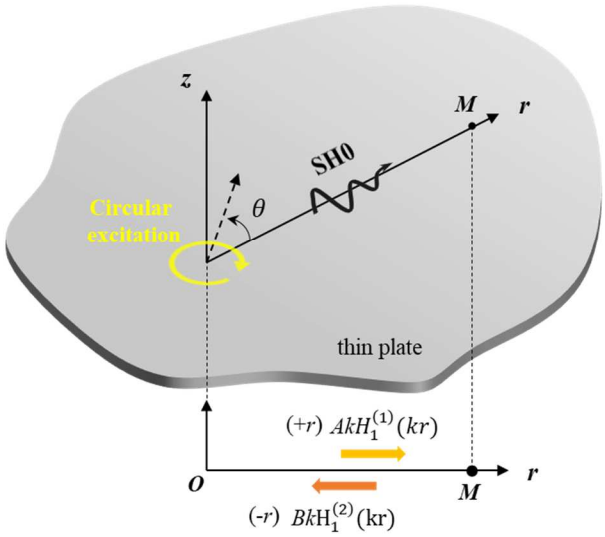

Fig. 2.1 Cylindrical coordinate system used for the analysis of the omnidirectional shear horizontal wave physics.

CHAPTER 3.
Meta-ring for enhancing emission efficiency of omnidirectional SH waves

3.1 Overview

The enhancement of transduction efficiency is a critical requirement for transducer development. A high transduction efficiency allows transducers to realize high detection accuracy, expanded inspection coverage, and reduced power consumption; further, it can be utilized effectively for non-destructive testing (NDT) and structural health monitoring (SHM). With regard to an inspection of a plate like structure, two types of transducers can be considered, unidirectional and omnidirectional. The former is powerful when performing a test in a specific direction, but in a tomography application, it requires a complicated measurement process to cover the full coverage of the angle. In contrast, omnidirectional transducers can detect a defect in a wide range of areas efficiently [1, 2]. However, it seriously suffers from the decreased output power of the emanated wave caused by an inverse square law attributed to the intrinsic physics of omnidirectionality. Therefore, the necessity for

research that boosts the output power of omnidirectional transducers is much more emphasized.

Meanwhile, three types of waves, such as out-of-plane symmetric [3-6] and antisymmetric [7-9] modes and in-plane shear horizontal mode [10-12] can be exploited for guided waves in a thin elastic plate. However, the fundamental shear horizontal wave mode (SH_0) is preferred because of its unique nondispersive characteristics [14, 22-27]. The wave dispersion induces a distortion or attenuation of the signal as the wave propagates over the distance and time. Furthermore, a lower distortion from external interfering causes and a higher detection resolution attributed to a shorter wavelength help to carry out an accurate inspection. Therefore, in-plane shear horizontal waves surpassed their out-of-plane counterparts (A and S modes) in practical advantages.

Several design methods have been considered to develop the omnidirectional SH wave transducers. Firstly, Seung et al. proposed an omnidirectional SH wave transducer based on a magnetostrictive effect [13] utilizing a strategy to match a wavelength with a patch size and a Lorentz force [14] with a unique magnetic circuit. Following these design methods, considerable works have been carried out depending on the types of transducer, including magnetostrictive patch transducers (MPT) with optimized magnetic circuits [15, 16] and the arrangement of more actuating elements [17-19], and electromagnetic acoustic transducers (EMAT) with specific magnet arrays [20, 21] to improve the transduction efficiency. On the other hand, Belanger and Bovin designed an omnidirectional SH piezoelectric transducer

using six trapezoidal d_{15}-mode PZT wafers [22]. After then, OSH-PTs using 12 trapezoidal face-shear PZT elements [23], thickness-poled [24-26] and radially poled [27] piezoelectric ring designs were developed to enhance the sensitivity in all directions. In addition, the influence of the properties [28] and the initial stress [29, 30] on the sensitivity of piezoelectric materials were also investigated. However, the suggested methods are confined to advancement at the internal design level, which is incompatible with other types and increases complexity, thereby deteriorating the practical usability. In short, a high-performance, compact, and robust form needs to be developed.

Mechanical metamaterials may show an alternative approach for improving the transduction efficiency of transducers. Artificially contrived unit cell structures are capable of manipulating mechanical constitutive wave properties into non-existing values, such as negative density and bulk modulus [31-40]. Based on these interesting characteristics, research has been conducted on various applications, including metasurface [41-47], extraordinary transmission [48, 49], and mode conversion [50-53]. Specifically, some recent studies related to the technique of wave collimation for enhancing wave intensity have been reported in acoustics and elastics. Hur et al. proposed a flat, thin layer piezoelectric ring array that forms a phase gradient metasurface for focusing the acoustic wave on achieving high resolution in water [43]. Lee et al. introduced an elastic metasurface for focusing in-plane longitudinal ultrasonic beams based on the substructured concept [40]. Cao et al. proposed an elastic SH wave focusing metasurface for enhanced sensing [46]. For

symmetric S, antisymmetric A, and surface Rayleigh modes in a thin plate, Tian et al. provided phased diffraction gratings for passive manipulating of focused guided wave beam to improve the signal to noise ratios [47].

The Purcell effect [54], which explains the modification of the spontaneous emission rate of quantum sources in a resonant cavity by modulating its surrounding environment, demonstrated a distinct approach. Since early discussions of this phenomenon began in quantum systems [55], subsequent concepts expanded macroscopically and drew interest in electromagnetics [56-58], acoustics [59-65], and elasticity [66-68]. In the acoustic case, Song et al. proposed double-walled metamaterial yielding Fabry-Perot resonance for emission enhancement of monopole sources [59]. Zhao et al. proposed an anisotropic structure preserving an omnidirectional [60] and highly directed to unidirectional or bidirectional [61] radiation with Mie resonance to achieve efficient emission of multiple acoustic sources. Furthermore, Landi et al. formulated a relation between an emission power enhancement and the acoustic density of states [62]. Liu et al. provided a rigorous analytical model to explain enhanced multipole emission of the sound [63]. Mei et al. proposed 'LEGO'-type acoustic metamaterial to enhance the low-frequency emission power [64]. Lei et al. proposed broadband emission enhancement with dual acoustic grating with anisotropic density [65]. In elasticity, Schmidt et al. showed an elastic analog of the Purcell effect with spherical nanoparticles serving as GHz antennas to modify the emission of the source [66]. However, those schemes cannot be directly applied to the ultrasonic transducers for an elastic waveguide carrying

two lamb wave modes and a shear horizontal wave mode. Recently, Kim et al. proposed the emission enhancement phenomenon of a unidirectional longitudinal wave transducer immersed in a near-zero impedance environment in a Fabry-Perot resonance using paired resonator [67]. A similar resonator structure was also studied for a flexural wave mode [68]. However, it should be directly attached to the MPT without compatibility with other types, and the inherent physics of the structure was not secured. Particularly, the physics considered for a one-dimensional, non-decaying plane wave in a plate does not apply to omnidirectional waves. Therefore, the feasibility of the conditions and configurations for the emission enhancement of the omnidirectional SH wave transducers remains in question.

In this study, we propose a theoretical model for enhancing the emission efficiency of the omnidirectional SH wave transducers using an externally designed single metamaterial ring (“meta-ring”). To deal with shear horizontal omnidirectionality, we simplify the complicated wave physics in cylindrical coordinates described with Hankel functions into the analytic system of a one-dimensional asymmetric problem. First, we replace the meta-ring with a discretized mass-spring model in an analytical form and rigorously analyze the gain function to confirm the boosting phenomena of the transducer. Then, we interpret an equivalent model of the meta-ring and illustrate that the enhancement phenomenon can be obtained at the frequency forming Fabry-Perot resonance cavity with a lowered impedance environment of the bounded system on which the transducer is placed. We also explicitly show that a high gain can be achieved at a Fabry-Perot resonance frequency inversely proportional to the

square root of the ratio of the effective impedance (~ $\sqrt{Z_0/Z_{eff}}$). We determine the design condition of the meta-ring based on the theoretical model to select the gain considering the tradeoff with bandwidth. Further, to validate our model, we design the meta-ring into a T-shaped beam that can exclusively perform the roles of the mass and spring parts. We used MPT for the omnidirectional SH wave transducer for the experiments, and its wave generation is modeled as an actuating source.

The numerical simulation results of the designed meta-ring buttress our theoretical model. Further, we experimentally confirm that the output shear strain measured in an omnidirectional shear horizontal magnetostrictive patch transducer (OSH-MPT) for sensing, as shown in Fig. 3.1(b), is increased by 269.3% compared to that for the conventional case without the meta-ring, as shown in Fig. 3.1(a). It should be mentioned that the proposed model is compatible with the existing transducer design methods and can passively boost transduction efficiency by installing a compact structure. We expect this approach will provide a breakthrough in overcoming the performance limitations of omnidirectional transducers.

3.2 Analysis of the physics in the meta-ring

We aim to establish a solid theoretical background for the meta-ring and transducer systems. We focus on developing a simplified equivalent model in axisymmetric coordinates to reduce the complexity of the analysis. Note that our system has no

variation along the circumferential direction; therefore, an axisymmetrically reduced bar model is apparently valid. Although our meta-ring system is compatible with a wide variety of transducer types, such as MPTs, EMATs, and PZTs, we especially employ OSH-MPT for shear horizontal wave generation considering their high omnidirectionality [13]. We first set up an equivalent excitation model for SH wave generation that simplifies the complicated deformation motion of the transducer to establish the analytic model. Then we introduce a discretized mass-spring model that elaborately translates the resonance motion of the meta-ring with a simplified mass m and stiffness s. We build a theoretical model to demonstrate the emission efficiency enhancement phenomenon of the meta-ring using the representative mass-spring system on the plate. In the last, we will contrive the equivalent effective medium model by substituting the meta-ring, and we interpret the mechanism of an abnormal enhancing phenomenon.

3.2.1 Wavefield equation of the transducer system with the meta-ring

In this analysis, the theoretical model consists of a discrete mass-spring system deforming in the circumferential direction attached to a single point of a bar with a nominal mechanical impedance Z_0 of a plate with thickness p_t. Here, the assumption that the structure functions as a point resonator is valid because the wavelength in

the frequency range of interest is much larger than the thickness of the structure. Now we investigate whether the wave transduction efficiency can be super-enhanced by attaching a meta-ring to the plate around the transducer.

To describe the wave motion in the axisymmetric one-dimensional bar model, we only consider the SH motion alone, and along with this, expressing the analytic mass-spring model working as a resonator is shown in Fig. 3.2(b). The resonator is modeled in mass m and stiffness s with the SH displacement of the mass part defined as um, attached at $r = W$. The SH displacement field in the bar is denoted as u_θ, and it varies along the medium $0 \le r \le a$, $a \le r \le W$, and $W \le r$. We used cylindrical coordinates to describe the wave equation (see Appendix A). The displacement u_θ in an axisymmetric bar model can be expressed in terms of the Hankel function as:

$$u_\theta = \begin{cases} A_1 k H_1^{(1)}(kr) + B_1 k H_1^{(2)}(kr) & (0 \le r \le a) \\ A_2 k H_1^{(1)}(kr) + B_2 k H_1^{(2)}(kr) & (a \le r \le W) \\ C k H_1^{(1)}(kr) & (W \le r) \end{cases} \tag{3.1}$$

where coefficients $A_i\,(i = 1,2)$ and C denote the amplitudes of the outward propagating wave components while $B_i\,(i = 1,2)$ denotes the amplitude of the inward propagating wave components. The symbol k denotes the wavenumber in the plate. As mentioned above, we omitted the frequency dependence $e^{i\omega t}$ for describing the displacement fields.

To satisfy the finite displacement condition at $r = 0$, the expression of the

displacement is rewritten using the Bessel functions of the 1st kind J_1 and 2nd kind Y_1 as follows:

$$u_\theta(r=0) = (A_1 + B_1)kJ_1(0) + i(A_1 - B_1)kY_1(0) \tag{3.2}$$

From Eq. (3.2), the coefficient of the 2nd kind of the Bessel function $Y_1(0)$ should be zero to avoid divergence of the displacement at the center; this can result in the condition $A_1 = B_1$.

At $r = a$, the displacement continuity and force equilibrium conditions are considered where an external force is applied. In this model, the exciting external force per unit length is given as $F_{trd,}$ and the internal force per unit length is written as $p_t\sigma_{r\theta} = p_t C_{66}\gamma_{r\theta} = Z_0 \frac{\omega}{k}\gamma_{r\theta}$, where p_t denotes the thickness and the stiffness C_{66} denotes the shear modulus of the elasticity of the plate and Z_0 denotes the characteristic impedance of the background medium given as $p_t\sqrt{\rho C_{66}}$ with the volume density ρ. Using these relations, we can get the displacement continuity and force equilibrium conditions as:

$$A_1 kH_1^{(1)}(ka) + B_1 kH_1^{(2)}(ka) = A_2 kH_1^{(1)}(ka) + B_2 kH_1^{(2)}(ka) \tag{3.3}$$

$$F_{trd} - Z_0\omega k\left(A_1 H_2^{(1)}(ka) + B_1 H_2^{(2)}(ka)\right) = -Z_0\omega k\left(A_2 H_2^{(1)}(ka) + B_2 H_2^{(2)}(ka)\right) \tag{3.4}$$

Similarly, at $r = W$, the mutual force f_m considering the interconnection between the mass-spring model and the waveguide can be calculated. In the model, the bottom part of the spring is attached to the plate at the point $r = W$, and the top part is connected to the center of the mass part. Therefore, the equation of motion for the

mass part with the displacement, which is denoted as u_m and mutual force, f_m, can be described as:

$$-\omega^2 m u_m = -f_m \tag{3.5}$$

$$f_m = s\left(u_m - u_\theta\left(r = W\right)\right) \tag{3.6}$$

The displacement continuity and force equilibrium conditions at $r = W$ is described as:

$$A_2 k H_1^{(1)}\left(kW\right) + B_2 k H_1^{(2)}\left(kW\right) = C k H_1^{(1)}\left(kW\right) \tag{3.7}$$

$$-f_m - Z_0 \omega k\left\{A_2 H_2^{(1)}\left(kW\right) + B_2 H_2^{(2)}\left(kW\right)\right\} = -Z_0 \omega k\left(C H_2^{(1)}\left(kW\right)\right) \tag{3.8}$$

By substituting Eq. 3.5 into Eqs. (3.6) and (3.7), the mutual force f_m is obtained as:

$$f_m = -\frac{s\omega^2}{s/m - \omega^2} C k H_1^{(1)}\left(kW\right) \tag{3.9}$$

From Eqs. (3.7-3.9), the reflection coefficient at $r = W$ is defined as $R \triangleq \frac{B_2}{A_2}$ and expressed in:

$$R = \left|R\right| e^{i\beta} = \frac{D\left(\omega\right) H_1^{(1)}\left(kW\right)}{H_2^{(2)}\left(kW\right) - D\left(\omega\right) H_1^{(2)}\left(kW\right) - \dfrac{H_2^{(1)}\left(kW\right) H_1^{(2)}\left(kW\right)}{H_1^{(1)}\left(kW\right)}} \tag{3.10}$$

with

$$D\left(\omega\right) \triangleq \frac{s\omega / Z_0}{\omega_r^2 - \omega^2} \tag{3.11}$$

where $\omega_r = 2\pi f_r = \sqrt{s/m}$ represents the resonance frequency of the mass-spring system and β denotes the phase of the reflection coefficient R. When the target

frequency ω is near the resonance frequency of the resonator, $D(\omega)$ in Eq. (3.11) goes to ∞, and therefore, the reflection coefficient R goes to -1. Total reflection occurs under this limit. It is important to examine the reflectance induced by the resonator in order to achieve a resonant cavity in the interior space of a metamaterial ring. We tuned the meta-ring to get a high reflection coefficient at the target frequency in this paper.

In the nominal case without the meta-ring, we can neglect the mass m (i.e., m = 0). Therefore, the ratio of the output coefficient of the shear horizontal displacement to the input force derived from Eqs. (3.1-3.4) is calculated as:

$$\frac{C_{nom}}{F_{trd}} = \frac{iJ_1(ka)}{Z_0\omega k}\frac{1}{Y_2(ka)J_1(ka) - Y_1(ka)J_2(ka)} \tag{3.12a}$$

$$u_{\theta,nom} = C_{nom}kH_1^{(1)}(kr) \tag{3.12b}$$

On the other hand, in the case of the meta-ring attaching to the waveguide, the ratio of the output coefficient to the input force is derived from Eqs. (3.1-3.4) and from Eqs. (3.7-3.11) is calculated as:

$$\frac{C_{meta}}{F_{trd}} = (1 + R\frac{H_1^{(2)}(kW)}{H_1^{(1)}(kW)})(\frac{1}{Z_0\omega k}\frac{iJ_1(ka)}{(1-R)\left(J_1(ka)Y_2(ka) - J_2(ka)Y_1(ka)\right)}) \tag{3.13a}$$

$$u_{\theta,meta} = C_{meta}kH_1^{(1)}(kr) \tag{3.13b}$$

Using the expressions in Eqs. (3.12a, b) and (3.13a, b), we can define the gain function $H(\omega)$ representing the signal output enhancement by the meta-ring as:

$$H(\omega) \triangleq \frac{C_{meta} / F_{trd}}{C_{nom} / F_{trd}} = \frac{1 + R\dfrac{H_1^{(2)}(kW)}{H_1^{(1)}(kW)}}{1 - R} \tag{3.14}$$

3.2.2 Wavefield equation of the equivalent system

This section investigates the physical implications of the proposed unique output enhancement through the meta-ring outlined in Section 3.2.1. We will first demonstrate that the installation of the meta-ring can dramatically reduce the effective impedance of the inner region surrounded by the resonator. The actuation frequency must be set to be equal to a Fabry-Perot resonance in order to transmit nearly all of the wave power from the inner region to the outer region, which has a mechanical impedance that is significantly different from that of the inner region. Lastly, we will show that the signal amplification is proportional to the inverse square root of the decreased impedance ratio of the effective medium region. For the analysis, we propose another equivalent bar model, depicted in Fig. 3.2(c), which consists of the outer original medium and inner effective medium of effective impedance Z_{eff} that is supposed to reflect the mechanical influence of the meta-ring. The length of the inner effective medium is redefined as W_{eff} for considering the edge effect of the meta-ring. Both the W_{eff} and Z_{eff} values are estimated using the transformed wave field.

The transformed displacement field $\tilde{u}$ in the equivalent system can be written in a

manner similar to that of the original system:

$$\tilde{u}_\theta = \begin{cases} 2k\tilde{A}_1 J_1(kr) & (0 < r \le a) \\ \tilde{A}_2 kH_1^{(1)}(kr) + \tilde{B}_2 kH_1^{(2)}(kr) & (a \le r \le W_{eff}) \\ \tilde{C}kH_1^{(1)}(kr) & (W_{eff} \le r) \end{cases} \tag{3.15}$$

where coefficients $\widetilde{A}_i\,(i=1,2)$ and $\widetilde{C}$ denote the amplitudes of the outward and inward propagating wave components in the inner effective medium while $\widetilde{B}_i\,(i=1,2)$ denotes the amplitude of the inward propagating wave components at the outer original medium. Here, the homogeneous effective medium for the equivalent system is considered to perfectly substitute the effect of the meta-ring on the original analytic model. However, as the wavenumber k unaffected by the transformation of the system, the only adjustable value for reflecting the phase shift in a homogeneous medium is the distance W_{eff}, which defines the boundary between the homogeneous medium of the effective impedance Z_{eff} and outer original medium of impedance Z_0.

To match the original and transformed fields, it is required that the coefficients $\widetilde{A_1}$, $\widetilde{A_2}$, $\widetilde{B_2}$, and $\widetilde{C}$ of the displacement $\widetilde{u_\theta}$ of the transformed field are related to the coefficients A_1, A_2, B_2, and C as,

$$\frac{\tilde{A}_i}{A_i} = \frac{\tilde{B}_i}{B_i} = g(\omega) \tag{3.16}$$

$$C = \widetilde{C} \tag{3.17}$$

$$\frac{\tilde{F}_{trd}}{F_{trd}} = h(\omega) \tag{3.18}$$

where $g(\omega)$ and $h(\omega)$ are the unknown functions to be determined. These functions should be properly determined for the field matching between the two systems. Obviously, the displacement field of the outermost propagating wave must be the same for the two models, as given by Eq. (3.17).

For the field matching at $r = a$ and $r = W_{eff}$ on the bar model, we explicitly write the displacement and traction boundary conditions as:

$$2k\tilde{A}_1 J_1(ka) = \tilde{A}_2 kH_1^{(1)}(ka) + \tilde{B}_2 kH_1^{(2)}(ka) \tag{3.19}$$

$$\tilde{F}_{trd} - 2Z_{eff}\omega k\tilde{A}_1 J_2(ka) = -Z_{eff}\omega k\left(\tilde{A}_2 H_2^{(1)}(ka) + \tilde{B}_2 H_2^{(2)}(ka)\right) \tag{3.20}$$

$$\tilde{A}_2 kH_1^{(1)}(kW_{eff}) + \tilde{B}_2 kH_1^{(2)}(kW_{eff}) = \tilde{C}kH_1^{(1)}(kW_{eff}) \tag{3.21}$$

$$-Z_{eff}\omega k\left(\tilde{A}_2 H_2^{(1)}(kW_{eff}) + \tilde{B}_2 H_2^{(2)}(kW_{eff})\right) = -Z_0\omega k\tilde{C}H_2^{(1)}(kW_{eff}) \tag{3.22}$$

If Eqs. (3.16) and (3.18) are substituted into Eq.(3.20), the resulting equation is compared with Eq. (3.4), and the relationship between $g(\omega)$ and $h(\omega)$ can be established as:

$$\frac{h(\omega)}{g(\omega)} = \frac{Z_{eff}}{Z_0} \tag{3.23}$$

In order to represent the external force applied by the transducer in an equivalent system, we argue that i) power P in the original system should be the same as that of the transformed system at $r = a$ and ii) power in the original system at $r = W$ should

be the same as that of the transformed system at $r = W_{eff}$, where $P = \mathrm{Re}\left\{F\dot{u}^*\right\}/2$.

Thus, at $r = a$,

$$P\left(r=a\right) = \widetilde{P}\left(r=a\right) \tag{3.24a}$$

where

$$P\left(r=a\right) = F_{trd}\omega\left|A_1\right| J_1\left(ka\right)\cos\left(\frac{\pi}{2}+\eta\right) \tag{3.24b}$$

$$\widetilde{P}\left(r=a\right) = F_{trd}\omega\left|A_1\right| J_1\left(ka\right)\cos\left(\frac{\pi}{2}+\eta+\theta-\gamma\right)\left|h\left(\omega\right)\right|\left|g\left(\omega\right)\right| \tag{3.24c}$$

In Eqs. (3.24a-c), the phases of the displacement coefficient A_1, and transformation functions $g(\omega)$ and $h(\omega)$ are denoted as η, θ, and γ, respectively, for a computational convenience. As a consequence of Eqs. (3.24a-c), the following relationship can be established:

$$\theta = \gamma \tag{3.25a}$$

$$\left|h\left(\omega\right)\right|\left|g\left(\omega\right)\right| = 1 \tag{3.24b}$$

Using Eqs. (3.23) and (3.25a-b), the two transformation functions can be derived as,

$$h\left(\omega\right) = \sqrt{\frac{Z_{eff}}{Z_0}}e^{i\theta}, g\left(\omega\right) = \sqrt{\frac{Z_0}{Z_{eff}}}e^{i\theta} \tag{3.26}$$

where θ is undetermined. Next, we consider the second power equivalence condition:

$$P\left(r=W\right) = \widetilde{P}\left(r=W_{eff}\right) \tag{3.27a}$$

where

$$P(r=W)=\frac{1}{2}\omega^2 Z_0\left|A_2 H_1^{(1)}(kW)\right|^2$$
$$=\frac{1}{2}\omega^2 Z_0\left|B_2 H_1^{(2)}(kW)\right|^2+\frac{1}{2}\omega^2 Z_0\left|CH_1^{(1)}(kW)\right|^2 \tag{3.27b}$$

$$\tilde{P}(r=W_{eff})=\frac{1}{2}\omega^2\,\mathrm{Re}(z)\left|\tilde{A}_2 H_1^{(1)}(kW_{eff})\right|^2$$
$$=\frac{1}{2}\omega^2\,\mathrm{Re}(z)\left|\tilde{B}_2 H_1^{(2)}(kW_{eff})\right|^2+\frac{1}{2}\omega^2 z_0\left|CH_1^{(1)}(kW_{eff})\right|^2 \tag{3.27c}$$

Substituting Eq. (3.26) into Eq. (3.27c) and solving Eqs. (3.27a-c) leads to the condition of effective impedance Z_{eff} as:

$$\mathrm{Re}(Z_{eff})=\left|Z_{eff}\right| \tag{3.28}$$

Eq. (3.28) implies that effective impedance is always positive and real-valued. Given Eqs. (3.21) and (3.22), the reflection coefficient $R_{equiv}=\tilde{B}_2/\tilde{A}_2$ at the impedance varying boundary at $r = W_{eff}$ can be derived as:

$$R_{equiv}=\frac{\frac{Z_{eff}}{Z_0}H_2^{(1)}(kW_{eff})-H_2^{(1)}(kW_{eff})}{-\frac{Z_{eff}}{Z_0}H_2^{(2)}(kW_{eff})+\frac{H_2^{(1)}(kW_{eff})H_1^{(2)}(kW_{eff})}{H_1^{(1)}(kW_{eff})}} \tag{3.29}$$

Using Eq.(3.16), the reflection coefficients R and R_{equiv} are same. Then, by substituting Eq. (3.10) into Eq. (3.29), we can obtain the effective impedance Z_{eff} as:

$$Z_{eff}=\frac{1+\frac{H_1^{(2)}(kW_{eff})}{H_1^{(1)}(kW_{eff})}R}{1+\frac{H_2^{(2)}(kW_{eff})}{H_2^{(1)}(kW_{eff})}R}Z_0 \tag{3.30}$$

where R is a reflection coefficient, defined in Eq. (3.10). Using Eqs. (3.28) and (3.30),

Z_{eff} and W_{eff} for the equivalent system can be numerically calculated.

When $kW_{eff} \gg 1$ is assumed, i.e., when the meta-ring is placed far away from the excitation source, the Hankel functions can be approximated as (see Appendix A.1):

$$H_{\alpha}^{(1)}\left(kW_{eff}\right) \sim \sqrt{\frac{2}{\pi kW_{eff}}} e^{i\left(kW_{eff} - \frac{\alpha\pi}{2} - \frac{\pi}{4}\right)} \tag{3.31a}$$

$$H_{\alpha}^{(2)}\left(kW_{eff}\right) \sim \sqrt{\frac{2}{\pi kW_{eff}}} e^{-i\left(kW_{eff} - \frac{\alpha\pi}{2} - \frac{\pi}{4}\right)} \tag{3.31b}$$

where α is the order of the Bessel functions. Substituting Eqs. (3.10) and (3.31a-b) into Eq. (3.30), one can express the effective impedance as

$$\frac{Z_{eff}}{Z_0} \approx \frac{1+|R|e^{iX}}{1-|R|e^{iX}} \tag{3.32a}$$

$$X = \beta - 2kW_{eff} - \frac{\pi}{2} \tag{3.32b}$$

Note that the magnitude of the reflection coefficient R appearing in Eq. (3.32a) is always smaller than or equal to 1 ($0 \le |R| \le 1$). Under this observation, the real-valuedness condition imposed on Z_{eff} as stated by Eq. (3.28), and X must be either $2n\pi$ or $(2n+1)\pi$ (n: integer). Therefore, Z_{eff} in Eq. (3.32a) becomes

$$i)\ for\ X = 2n\pi;\quad \frac{Z_{eff}}{Z_0} = \frac{1+|R|}{1-|R|} > 1 \tag{3.33a}$$

$$i)\ for\ X = (2n+1)\pi;\quad \frac{Z_{eff}}{Z_0} = \frac{1+|R|}{1-|R|} < 1 \tag{3.33b}$$

In this study, we used the results in Eq. (3.33b) because a lowered effective

impedance can yield a higher gain of the output displacement.

Next, the relation between effective impedance and gain will be explored. From Eqs. (3.7) and (3.27b), the following relation can be derived:

$$\left|1+R\frac{H_1^{(2)}(kW)}{H_1^{(1)}(kW)}\right|=\sqrt{1-|R|^2} \tag{3.34}$$

Then, the magnitude of the gain function as derived in Eq. (3.14) can be rewritten using Eqs. (3.10) and (3.34) as:

$$\max|H(\omega)|=\max\left(\frac{\sqrt{1-|R|^2}}{\sqrt{1+|R|^2-2|R|\cos\beta}}\right) \tag{3.35}$$

Examination of Eq. (3.35) indicates that the magnitude of the gain function can be amplified when the phase of the reflection coefficient β is set as $\cos\beta=1$. Then, we substituted this condition into Eqs. (3.32b), (3.33b), and Eq. (3.35) to obtain

$$\cos(2kW_{eff}+\frac{3}{2}\pi)=1 \tag{3.36a}$$

$$\max|H(\omega)|=\sqrt{\frac{1+|R|}{1-|R|}}=\sqrt{\frac{Z_0}{Z_{eff}}} \tag{3.36b}$$

$$W_{eff}=\frac{c_s}{2f}(n-\frac{3}{4}),\ n=1,2\ldots\ \left(c_s\text{: the phase velocity of the SH wave}\right) \tag{3.36c}$$

From the result of Eq. (3.36b), we can now argue that to maximize the magnitude enhancement using the meta-ring, the ratio of the effective impedance of the equivalent system to the impedance of the original system should be as small as possible. At least, it should be smaller than unity. Furthermore, Eq. (3.36b) suggests

that the higher the reflection coefficient is, the larger the magnitude of the gain becomes.

It is argued that Eq. (3.36a) represents the Fabry-Perot condition for the resonant cavity of omnidirectional SH wave in the cylindrical coordinate system. Although the transduction efficiency should be decreased due to the high reflection caused by the impedance mismatch between the inner medium of the lowered effective impedance and the outer normal medium, at that frequency, full transmission is possible because the selected frequency is one of the Fabry-Perot resonance frequencies.

3.3 Design of meta-ring with analytic and FEM simulation

To realize high output enhancement by the proposed meta-ring, we designed a meta-ring and examined its frequency response using finite element simulations. Specifically, we designed the meta-ring structure as a ring type T-shaped cross-sectional beam that can function as a resonator at a specified frequency. Referring to Fig. 3.2(a), s_x = 2 mm, s_y = 3 mm, m_x = 6 mm, m_y = 3 mm and W = 52 mm. It is made of aluminum (Young's modulus E = 70 GPa, Poisson's ratio ν = 0.33, and density ρ = 2700 kgm^{-3}. The meta-ring is designed to simulate the discretized mass-spring model such that its top part works merely as a mass, and its bottom part works as a spring. The finite element analysis results indicate that the mass and stiffness of the

structure are evaluated as m = 14.7 g and s = 3.819 GNm^{-1}, respectively, with the lowest shear horizontal eigenfrequency f_{res} = 81.112 kHz (will be discussed in Section 3.3.3). The meta-ring is installed on the waveguide, an aluminum plate with a thickness p_t = 1 mm, and therefore, the nominal impedance and phase velocity of the shear horizontal wave in the plate are Z_0 = 8429.3 kgs^{-1} and c_s = 3122ms^{-1}, respectively. For the size of the annular type magnetostrictive patch, the representative radius a = 15 mm is selected.

3.3.1 Analysis results of the transduction efficiency enhancement using the meta-ring

According to the selected geometric parameters, the frequency responses of the normalized output displacements fields $\left|u_\theta / u_{\theta,nom}^{\max}\right|$ and the enhancement gain function $\left|H(\omega)\right|$ defined in Eqs. (3.12a,b), (3.13a,b), and (3.14) are presented in Fig. 3.3(a) and 3.3(b). Here, the target frequency f_t is designated when the maximized output displacement field $\left|u_\theta\right|$ of the nominal case is gauged. At $f = f_t$, $\left|H(\omega)\right|$ increased to 329.8%, which indicates that the displacement field $\left|u_\theta\right|$ is highly amplified when the meta-ring is installed, in comparison to the maximum displacement $\left|u_{\theta,nom}^{\max}\right|$ of the nominal case without the meta-ring. Also, Fig. 3.3(c) and 3.3(d) show the magnitude and phase angle of the reflection coefficient defined

in Eq. (3.10) on a frequency domain. It is clearly shown that the meta-ring yields high reflectance around the target frequency, indicating the possibility of achieving a resonant cavity circumstance inside. When the frequency is tuned to f_{res}, it is apparent that the mass-spring model works as a dynamic absorber or a perfect wave reflector. Therefore, the meta-ring perfectly drops off the gain $|H(\omega)|$ to 0 with the reflection coefficient R of magnitude 1 and phase angle π.

The effective parameters Z_{eff} and W_{eff} of the equivalent system in the frequency domain are plotted in Figs. 3.4(a) and 3.4(b). Fig. 3.4(a) shows that Z_{eff}/Z_0 converges to 0 as the frequency approaches f_{res}. Further, Fig. 3.4(a) also shows the asymptotic solution of the Z_{eff}/Z_0 based on Eqs. (3.31) ~ (3.33), which are plotted as dotted lines. Fig. 3.4(c) shows that at $f = f_{res}$, $|H(\omega)|$ becomes zero, for which the reflection coefficient R becomes -1. The complete form of the effective impedance can be expressed in two types as Eqs. (3.33a,b): the impedance increased case $Z_{eff}/Z_0>1$ with a phase condition of $\beta - 2kW_{eff} = (2n+1/2)\pi$ and the impedance lowered case $Z_{eff}/Z_0< 1$ with a phase condition of $\beta - 2kW_{eff} = (2n+3/2)\pi$; the latter case is utilized in this research to facilitate the enhancement of the transduction efficiency of the wave. However, simply lowering the effective impedance aggravates the impedance mismatch at the interface, which reduces the transduction efficiency. Therefore, an enhancement can be achieved at the frequency tuned to be the Fabry-Perot resonance frequency; this is induced by the phase condition of the phase of the reflection coefficient in Eq. (3.36a). The selected target frequency f_t is set to this

Fabry-Perot resonance frequency of the equivalent medium confined in $r = W_{eff}$ and effective impedance Z_{eff}. Thus, following Eq. (3.36b), the maximum enhancement gain function achieved at $f = f_t$ can be rewritten as the inverse square root of the impedance ratio, as indicated in Fig. 3.4(c).

3.3.2 Effects of meta-ring location and resonance frequency

The effects of distance W and resonance frequency f_{res}, two key parameters specifying the meta-ring, are investigated based on the rigorously analyzed theoretical model of the meta-ring. For the investigation, the contour plot of the gain function $H(\omega, W)$ is presented in Fig. 3.5(a) on the plane of frequency $f\,(=\omega/2\pi)$ and distance W. In this figure, two sets of lines are observed: i) oblique lines tracing high gains and ii) a vertical line indicating the resonance frequency. The pattern or shape of the latter line is barely affected by the change of W (see the detail in Section 3.3.3). Next, each of the oblique gain lines corresponds to a set of solutions satisfying the Fabry-Perot resonance condition derived in Eq.(3.36c) for n = 1, 2, and 3. They are denoted by 1st, 2^{nd,} and 3rd FP in Fig. 3.5(a); apparently, the Fabry-Perot resonance phenomenon is governed by the radius W of the meta-ring, and therefore, W critically affects the peak frequency. We can select the value of W along the FP lines to attain the maximum gain at the target operating frequency of the transducer.

On the other hand, to select f_{res} through the specific structural geometries, the effects of f_{res} on the system are also examined. f_{res} should be designated near f_t because we utilize the resonance phenomenon of the meta-ring to enhance the transduction efficiency. To confirm the relation between f_{res} and f_t, we draw the equi-W lines for W = 48 mm, 52 mm, and 56 mm, respectively, as shown in Fig. 3.5(b). As f_t is closer to f_{res}, a higher gain can be achieved with a narrower gain bandwidth. Effective impedance Z_{eff} can be considerably lower because the magnitude of the reflection coefficient radically approaches 1 at a frequency close to f_{res}. In addition, we should properly select f_{res} considering the amplitude and bandwidth of the enhancement gain at $f = f_t$ because the gain goes 0 at $f = f_{res}$, as discussed in Section 3.2.2. For this reason, we examined the design condition of distance W to determine the gain, full width at half maximum (FWHM), and target frequency of the meta-ring.

Fig. 3.5(c) shows a trade-off between the gain and FWHM along the variation in distance W on the 2nd FP line. In addition, Fig. 3.5(d) shows the variation in distance W of the target frequency f_t normalized to the resonance frequency f_{res}. Following this result, we can select f_t by considering the f_{res} of the meta-ring. Considering the actual fabrication, W = 52 mm is selected for the meta-ring. Based on our theoretical model, the design conditions of the meta-ring with a certain cross-section and radius of structure make it feasible to obtain gain enhancement $|H(\omega, W)|$ at the desired f_t.

3.3.3 Finite element analysis to design the meta-ring structure

The eigenmode and static deformation analyses are conducted to configure the meta-ring, which is modeled in a T-shaped cross-sectional beam structure. From the data of its eigenfrequency f_{res}, and asymmetric shear horizontal displacement u_θ under static shear force, the distributed mass m and stiffness s of the structure can be estimated. For the convenience of estimation, a slice of the structure conditioned with anti-symmetry along the circumferential direction is used. Using the geometry parameters mentioned in Section 3.3.1, the eigenfrequency is obtained as 81.112 kHz with the lowest shear horizontal eigenmode of the structure, whose motion is dominant in the circumferential direction, as shown in Fig. 3.6(a). Although W is modified, the eigenfrequency of the structure remains approximately unchanged, as depicted in Fig. 3.6(b). Besides, we can observe that the bottom and top parts work as the spring and mass of a mass-spring system in the eigenmode shape.

For this reason, as illustrated in Fig. 3.6(c), the static structural deformation analysis allows for the evaluation of stiffness s through displacement under a unit force applied to the mass part. In detail, the shear horizontal displacement of the mass part u_θ under a prescribed unit force uniformly distributed to the head of the mass part is estimated. Thus, the stiffness value s is evaluated as 3.819 GNm^{-1}, and therefore, mass m calculated as $s/(2\pi f_{res})^2$ is 14.7 g under the distance variable W = 52 mm. The stiffness of the meta-ring structure varies considerably with the changes in distance W, as indicated in Fig. 3.6(d). Generally, to define the stiffness of a structure

in cylindrical coordinates, one can denote the moment equilibrium relation as follows:

$$M_t = G\frac{d\phi}{dz}I_z \tag{3.37}$$

where M_t denotes a moment loaded onto the circular structure, G is the shear modulus, $\frac{d\phi}{dz}$ denotes a ratio of twist, and $I_z = \frac{1}{2}\int_A r^2 dA$ denotes the polar moment of the inertia. Here, we assume that the ratio of twists is made evenly in the height direction. Considering the relationship to the proposed meta-ring structure, we show that each term of Eq. (3.37) is calculated as

$$M_t = V \times W \tag{3.38a}$$

$$I_z = \pi\left(m_x + s_x\right)W^3 \tag{3.38b}$$

$$\frac{d\phi}{dz} = \frac{\Delta\phi}{m_y + s_y} \tag{3.38c}$$

where V represents the fixed value and denotes the integration of the shear horizontal force along the circumferential direction of the structure. From Eqs. (3.37) and (3.38 a-c) with the description of displacement u_θ written in $W\Delta\phi$, the theoretical shear stiffness s_{theory} is given as

$$s_{theory} = \frac{V}{u_\theta} = \frac{\pi\left(m_x + s_x\right)}{m_y + s_y}GW \quad . \tag{3.39}$$

The result of Eq. (3.39) points out that the stiffness of the structure is theoretically proportional to the distance variable W. Furthermore, we assume that the top part

will play a dominant mass role, so we can calculate the theoretical mass m_{theory} as

$$m_{theory} = \rho \cdot 2\pi W m_x m_y \quad . \tag{3.40}$$

Combining Eqs.(3.39) and (3.40), the theoretical resonance frequency of the structure can be calculated as

$$f_{res}^{theory} = \frac{1}{2\pi}\sqrt{\frac{s_{theory}}{m_{theory}}} = \frac{1}{2\pi}\sqrt{\frac{G(m_x + s_x)}{2\rho m_x m_y (m_y + s_y)}} \quad . \tag{3.41}$$

Eq.(3.41) reveals that the resonance frequency can be tuned independently to the distance variable W. Using the given geometry parameters, s_{theory}, m_{theory}, and f_{res}^{theory} are calculated as 5.732 GNm^{-1}, 15.9 g, and 95.56kHz, respectively. It can be confirmed that the theoretically estimated values were larger than the actual values estimated by finite element analysis. The reason for the error is that in the process of theoretically interpreting the structure, the mass of the spring part, the relative displacement of center of the mass, and the actual unevenness of the rate of twist were ignored. However, using the theoretical model, we can predict the order of mass and stiffness, and select independent variables f_{res} and W.

3.3.4 Numerical simulations for transduction efficiency enhancement by meta-ring

We conducted FEM harmonic simulations using COMSOL Multiphysics 5.3 to validate the established analysis model. A three-dimensional full model of the

transducer system with the meta-ring attached to the aluminum plate of thickness p_t was reduced to a circular sectional model of the angle $\theta = 5^\circ$, as depicted in Fig. 3.7(a), to reduce the computational cost. Additionally, the asymmetric continuity condition was applied to radial lines so that the reduced model could represent the pure in-plane omnidirectional SH wave. The wave generation of the MPT was represented as an external force, F_{trd}, which was equally prescribed in the circumferential direction, and alternatively at $r = a_1$ and $r = a_2$. The perfectly matched layers (PMLs) were applied to the outer medium outside boundary A.

As demonstrated in Fig. 3.7(b), the finite element analysis results for the enhancement gain using a meta-ring as functions of f and distance W. We confirm that similar FP lines based on the numerical simulation are in good agreement with the theoretical result of Fig. 3.5(a). To compare the detailed frequency response and wave motion of the model with the theoretic result, we drew an equi-W line for W =52 mm, as described in Section 3.3.2 and as depicted in Fig. 3.7(c). The FEM simulation result shows a similar enhanced gain at a slightly altered peak frequency of f_{peak}^{FEM} = 68.7 kHz from the theoretical prediction of f_{peak}^{theory} = 69.9 kHz. Indeed, the developed theoretical model was in good agreement with the FEM simulation. The discrepancy between the FEM simulation and theoretical result can be explained by the geometrical discontinuity arising from the meta-ring structure along the radial direction. Besides, the von-mises stress field results of the FEM simulation at the peak frequency of 68.7 kHz are presented in Fig. 3.7(d). The wave was highly

concentrated in the medium of the meta-ring due to the Fabry-Perot resonance phenomenon and significantly increased outside of the meta-ring by 314.5% compared to the conventional model. This is because the meta-ring has high reflectivity at the target frequency. In particular, while satisfying the Fabry-Perot condition at the target frequency, the phases of the reflected waves become the same and overlap in the interior.

3.3.5 Numerical simulations to investigate effects of input signal cycles

We conducted transient analysis using FEM simulation to confirm the effectiveness of the meta-ring in regard to the driven signal cycle and the signal to noise ratio. Because the theoretical foundation on the meta-ring is based on a full harmonic condition, the transduction efficiency of the meta-ring is reduced with the number of the input signal cycle not sufficient. To investigate the effects of the cycle number of the input sine wave on the signal amplification, the following 4 input signals are considered: Hanning-windowed 10-cycle sine wave, 30-cycle sine wave, 50-cycle sine wave, and 100-cycle sine wave. For the analysis, the FEM simulation model used in Section 3.3 is employed. Fig. 3.8 shows the output shear horizontal displacement signals measured with and without the meta-ring. The gain was defined as the maximum peak-to-peak amplitude for the entire output wave signal. The

results show that the amplification ratios are 27.8%, 171.7%, 265.3%, and 276.1%, respectively, for the considered 4 input signals. This suggests that meaningful wave amplification can be possible if the input number of cycles is over 30. It also shows that the input number of cycles over 100 shows full performance corresponding to the harmonic condition. Figure 3.9 shows a snapshot of the transient analysis result when the input signal of a 100-cycle sine wave is given.

Fig. 3.10 shows the transient analysis results for the input signal of a 100-cycle sine wave of shear horizontal displacement. To see any adverse effect of the meta-ring installation, such as the generation of unwanted wave modes, e.g., the Lamb wave mode, the output SH and the Lamb waves (corresponding to the out-of-plane displacement) are calculated by the finite element. The results in Fig. E2 show that the amplitude of the out-of-plane displacement signal corresponding to the Lamb wave is negligibly small compared to the SH displacement.

3.4 Experimental validation

We fabricated a prototype and conducted wave experiments to evaluate the performance of the meta-ring in boosting the transduction efficiency of the theoretically modeled transducer supported by FEM simulation. Fig. 3.10(a) shows the experimental setup, the ring installed on the diagonal of a 1 mm-thick aluminum alloy plate 1.2 m×1.2 m in size. The rest of the geometry and material properties are the same as those used in Section 3. In the experiments, we used annular type

magnetostrictive patch transducers (MPTs) as an actuator and a receiver that generated the lowest shear horizontal wave (SH0) considering their uniform omnidirectionality [13]. Further, we elaborately installed a meta-ring aligned with the center of the actuator MPT using an epoxy (DP-100). In addition, we attached the dissipative material (Blu-tack) in a rectangular shape that includes the sensor and actuator to prevent interruption owing to the reflection signals at the boundaries.

The experimental procedure is briefly described as follows (the detailed algorithm is shown in Appendix D). First, we generate a sine function signal of 100 cycles using a function generator (see Appendix E). The generated signals have varying center frequencies ranging from 50 kHz to 80 kHz. The frequency resolutions are 0.1 kHz between 62 kHz and 65 kHz and 1 kHz elsewhere. The generated signals by the function generator were amplified through a power amplifier (AG1017L) and inputted to the actuating OSH-MPT, which excites an omnidirectional SH0 wave in the test plate. Then, the receiving OSH-MPT located 1.2 m away from the actuating MPT picked up the voltage signals of the omnidirectional SH0 waves, which propagated in the plate. The measured voltage signal was amplified by a preamplifier (SR560) and stored at an oscilloscope (LeCroy Waverunner 104MXI) for further signal processing. Next, we installed the meta-ring around the actuator MPT and carried out the above measurement process equally. Because the measured voltage was proportional to the magnitude of the shear strain $|S|$, the peak-to-peak voltage values were extracted and divided by each correspondence frequency data to estimate the enhancement gain at a frequency range of 50 to 80kHz, including the

target frequency f_t = 69.9 kHz as predicted.

As shown in Fig. 3.10(b), the experimentally estimated enhancement gain function $|H(\omega)|$ of the meta-ring is plotted as red circles. The results indicate that the meta-ring enhances the output signal magnitude by the meta-ring-installed OSH-MPT by as much as 269.3% at the frequency $f_{peak}^{\exp}$ = 63.5 kHz when compared with the output signal by the OSM-MPT without a meta-ring. The finite element result shown in Fig. 3.10(b) was adjusted to reflect the unavoidable damping effects of the epoxy resin layer used to bond the MPT transducer to the test plate. Table 1 presents a more quantitative comparison of the two results. There is a slight discrepancy in the frequency of the maximum output signal between the numerical and experimental results; this can be attributed to some fabrication errors and the effects of the presence of epoxy bonding. However, the proposed principle of output signal enhancement by the meta-ring functions as predicted.

3.5 Summary

Concerning ultrasonic transduction efficiency enhancement of omnidirectional SH waves, we proposed a non-conventional method using a frequency-tuned circular ring, a meta-ring, devised based on a metamaterial concept. Because it is directly installed onto a test structure, a plate in the present study, the proposed approach contrasts with conventional approaches that mainly focus on the reconfiguration of

transducers. Furthermore, the proposed approach is cost-effective and, more importantly, offers a possibility of additional emission enhancement gain.

For the new development of the wave enhancing meta-ring, we should lower the effective impedance of the excited region of the plate by a transducer and overcome the resulting impedance mismatch by Fabry-Perot resonance. To lower the effective impedance of the transducer-excited zone, which is the main challenge, we theoretically investigate the impedance lowering mechanism and its relation with emission enhancement using our one-dimensional analysis model. Also, our formalism was confirmed numerically and experimentally.

It was shown that the proposed meta-ring reduces the impedance of the zone of interest to 9.18% of the base plate impedance at a target frequency of 69.9 kHz, for which the meta-ring is designed to have its resonance frequency at 81.1 kHz. The resulting output enhancement was 329.8% theoretically and 269.3% experimentally. When a finite-cycle signal is given, we cannot expect a 100% enhancement capacity of the meta-ring. This is because in theory, the proposed meta-ring functions under harmonic waves. To be able to use a short toneburst signal, some additional studies, such as meta-ring design optimization, which is beyond the scope of this study, would be needed. Since omnidirectional waves are crucial for wide-area ultrasound imaging, the proposed meta-ring is expected to advance omnidirectional-wave-based non-destructive testing techniques.

Table 3.1 Peak frequency and gain results of the theoretical model/FEM/FEM+bonding simulation and experiment.

	Theory	**FEM**	**FEM+bonding**	**Experiment**
f_{peak} [kHz]	69.9	68.7	63.8	63.5
Gain [%]	329.8	314.5	278.5	269.3

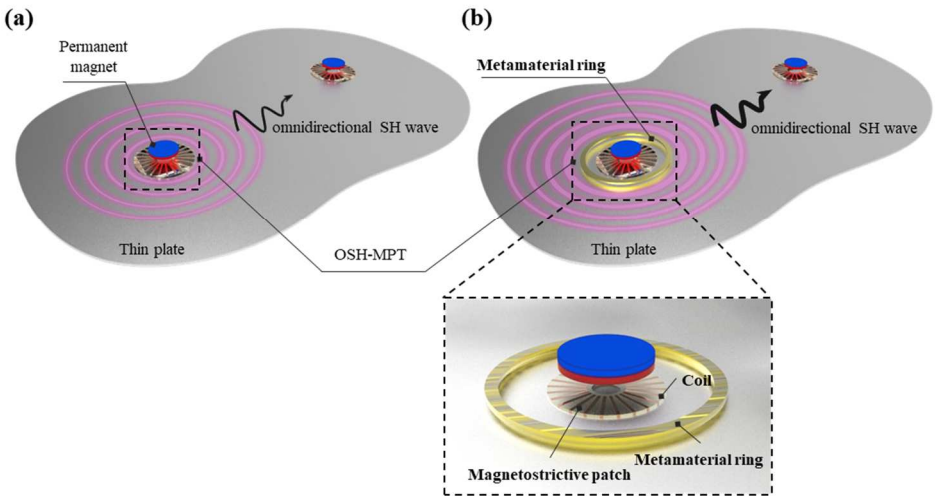

Fig. 3.1 Schematics of the meta-ring model with OSH-MPTs. (a) Illustrations of an actuated wave signal generated by a transducer decreasing inverse squarely due to omnidirectionality and (b) a boosted wave signal when a meta-ring is attached.

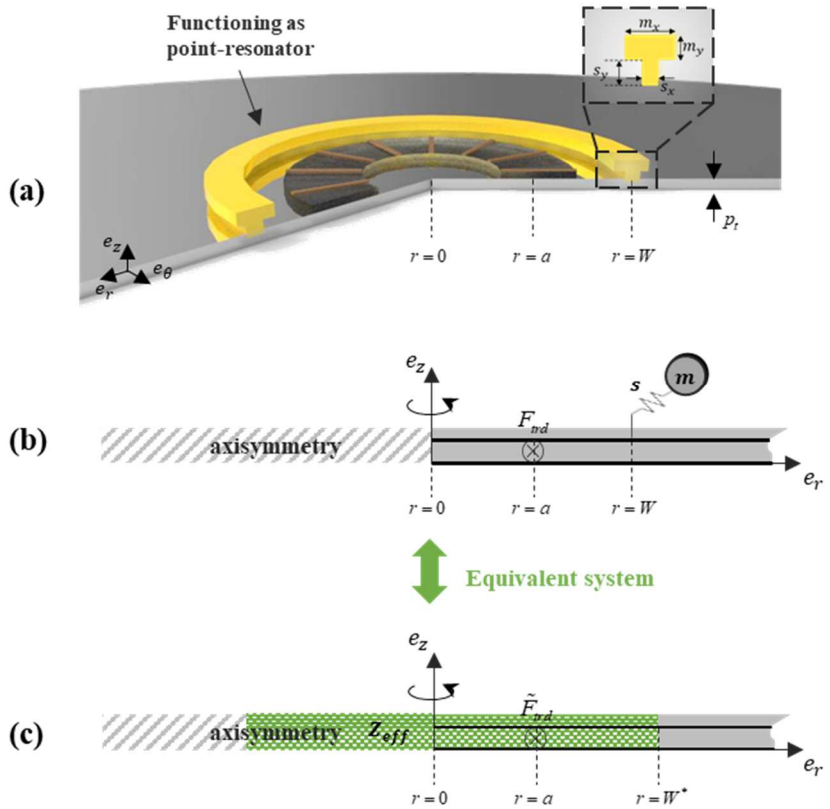

Fig. 3.2 (a) Proposed theoretical model for the meta-ring with a transducer. The detailed geometric dimensions of the meta-ring structure in the T-shaped beam are s_x = 2 mm, s_y = 3 mm, m_x = 6 mm, m_y = 3 mm, and the test plate thickness p_t = 1 mm. (b) One-dimensional model depicting the axisymmetric plate as a bar and the meta-ring as a mass-spring resonator. (c) A homogenized equivalent model with the mechanical effects of the meta-ring smeared in the bar where the zone affected by the meta-ring is assumed to have an effective impedance Z_{eff}. The symbol $\widetilde{F}_{trd}$ represents the resultant pin-forces generated by the magnetostrictive patch.

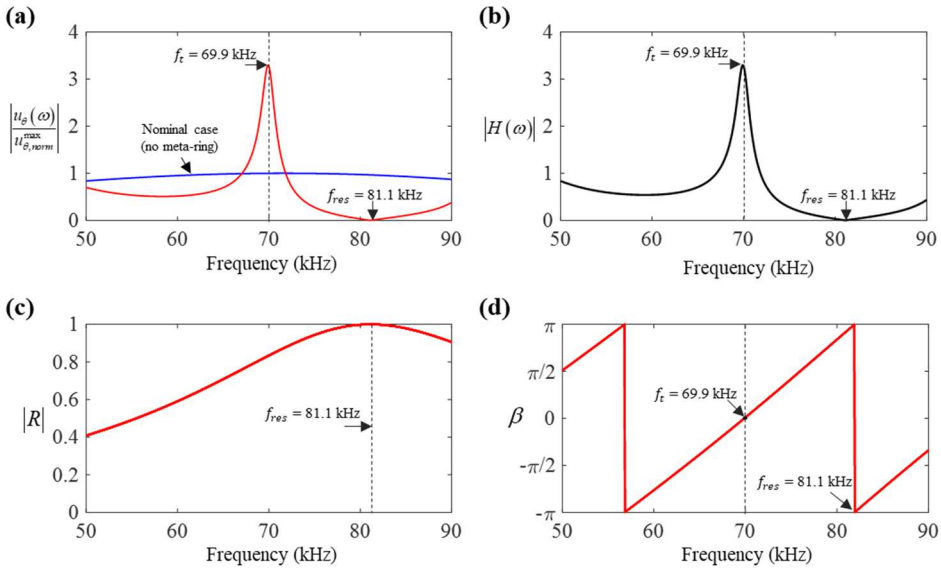

Fig. 3.3 Analytic solutions of the SH wave in a bar with a mass-spring model as a function of frequency. (a) Radiated displacement field $|u_\theta|$ of the nominal and meta-ring attached cases. (b) Enhancement gain function $|H(\omega)|$ of the meta-ring. (c) Magnitude and (d) phase of the reflection coefficient at the boundary of the mass-spring model.

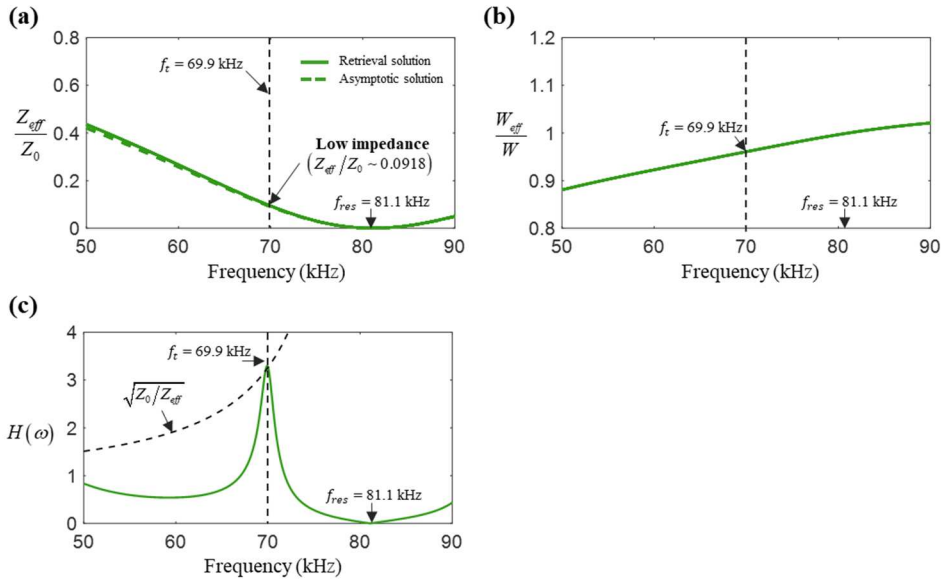

Fig. 3.4 Analytic solutions of the SH wave in an equivalent bar system as a function of frequency. (a) Ratio of effective impedance to nominal impedance Z_{eff}/Z_0 through the retrieval and asymptotic solution and (b) effective distance W_{eff}. (c) The explicit enhancement gain function $|H(\omega)|$ with an asymptotic dotted line of the inverse square root of the impedance ratio.

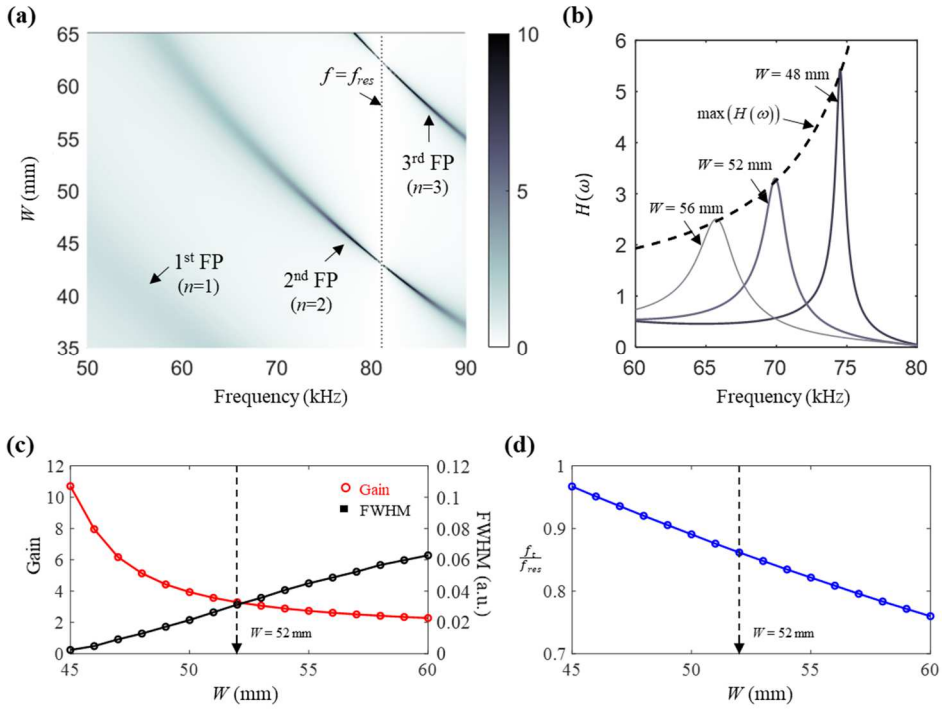

Fig. 3.5 (a) Contours of the enhancement gain $|H(\omega,W)|$ as functions of the frequency *f* and distance *W* under fixed geometries of the T-shaped cross-section of the meta-ring. (b) $|H(\omega)|$ as a function of frequency *f* along the equi-*W* lines for *W* = 48 mm, 52 mm, and 56 mm. (c) Gain and full width at half maximum along the distance *W* of the meta-ring. (d) Variation of the normalized target frequency along the distance *W*.

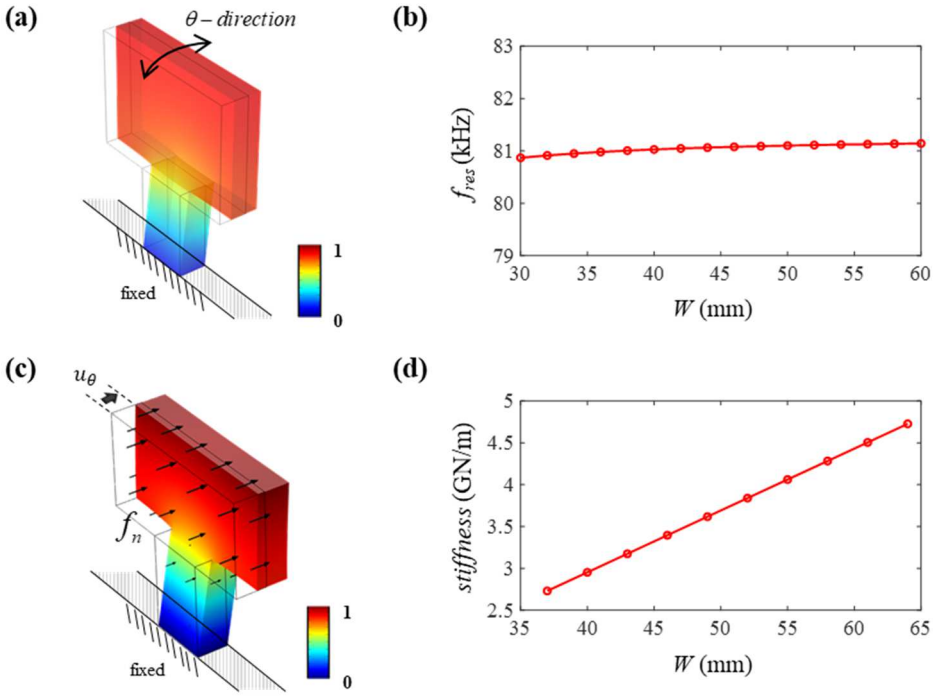

Fig. 3.6 Finite element analysis to extract mass *m* and stiffness *s* of the meta-ring structure. (a) SH eigenmode of the meta-ring fragment and (b) varying eigenfrequency of the structure along the change in variable *W*. (c) Angular deformed shape of the meta-ring fragment under an applied force (f_n) perpendicular to the cross-section and (d) the varying stiffness of the structure along the change in the distance variable *W*.

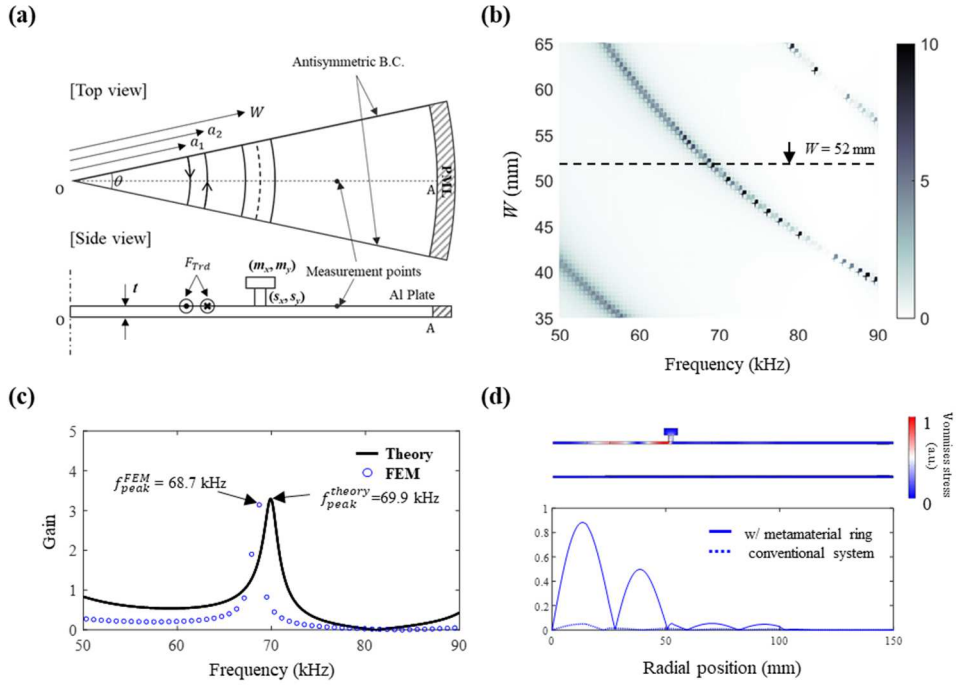

Fig. 3.7 (a) Finite element model for verifying an effect of the meta-ring structure under harmonic conditions. (b) Parametric sweep analysis on variables *W* and frequency *f* to find a boosting phenomenon. (c) Comparison of the theoretical/FEM simulation results of the enhancement gain function $|H(\omega)|$ using the meta-ring. (d) Normalized von-mises stress fields in the FEM simulation results for the conventional transducer system and the transducer boosted with the meta-ring at a peak frequency of 68.7 kHz.

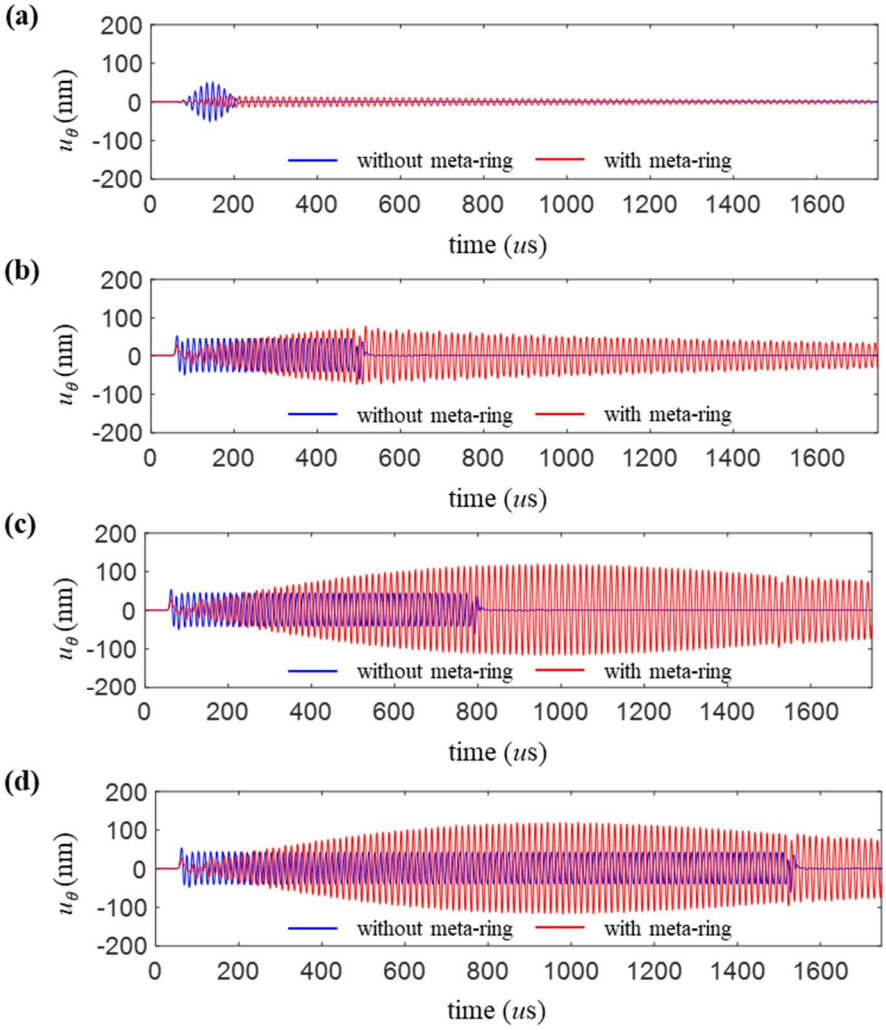

Fig. 3.8 The output shear horizontal displacement signals are predicted by the transient analysis. The considered input signals are (a) the Hanning-windowed 10-cycle sine wave, (b) 30-cycle sine wave, (c) 50-cycle sine wave, and 100-cycle sine wave.

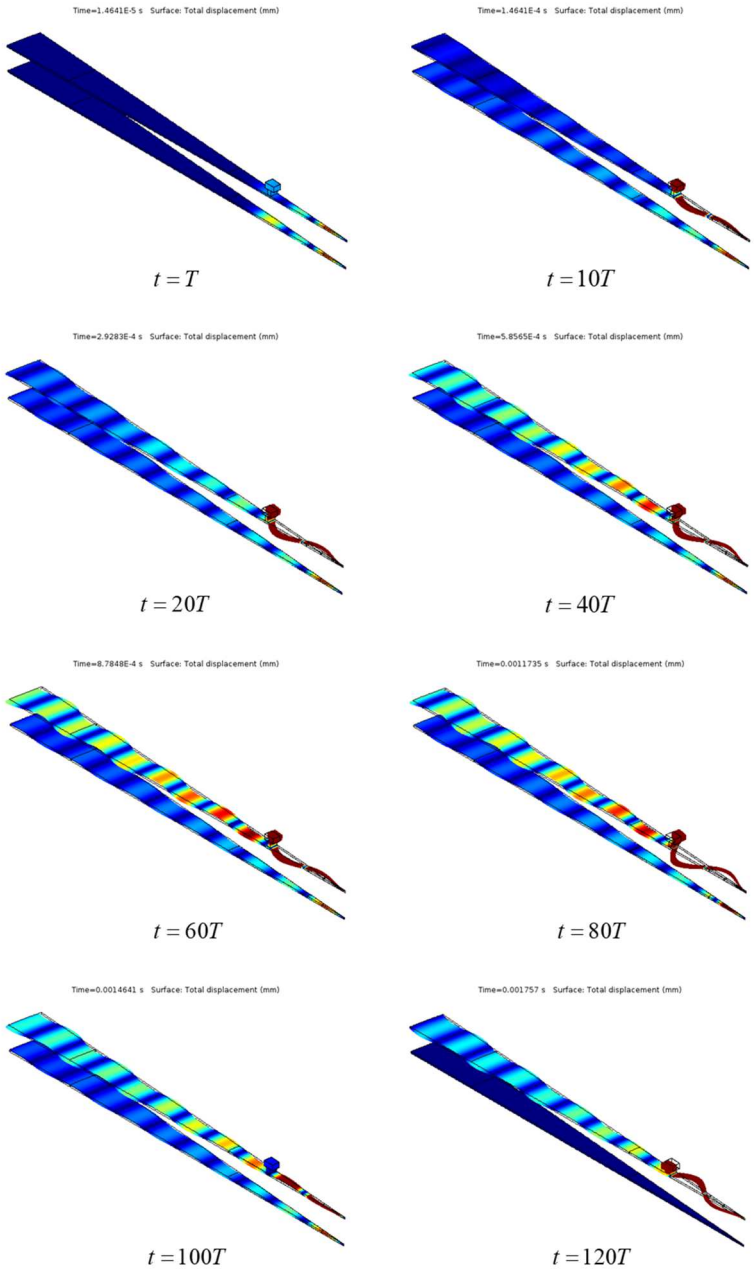

Fig. 3.9 Snapshots from animated images of the transient analysis using 100-cycle sine wave inputs.

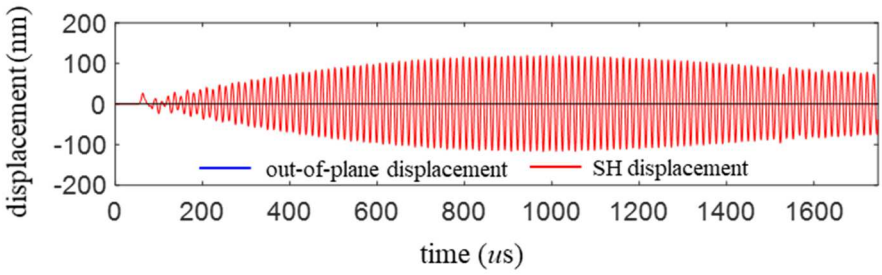

Fig. 3.10 The output displacement signals corresponding to the SH and the Lamb waves (corresponding to the out-of-plane displacement) are calculated by the finite element analysis

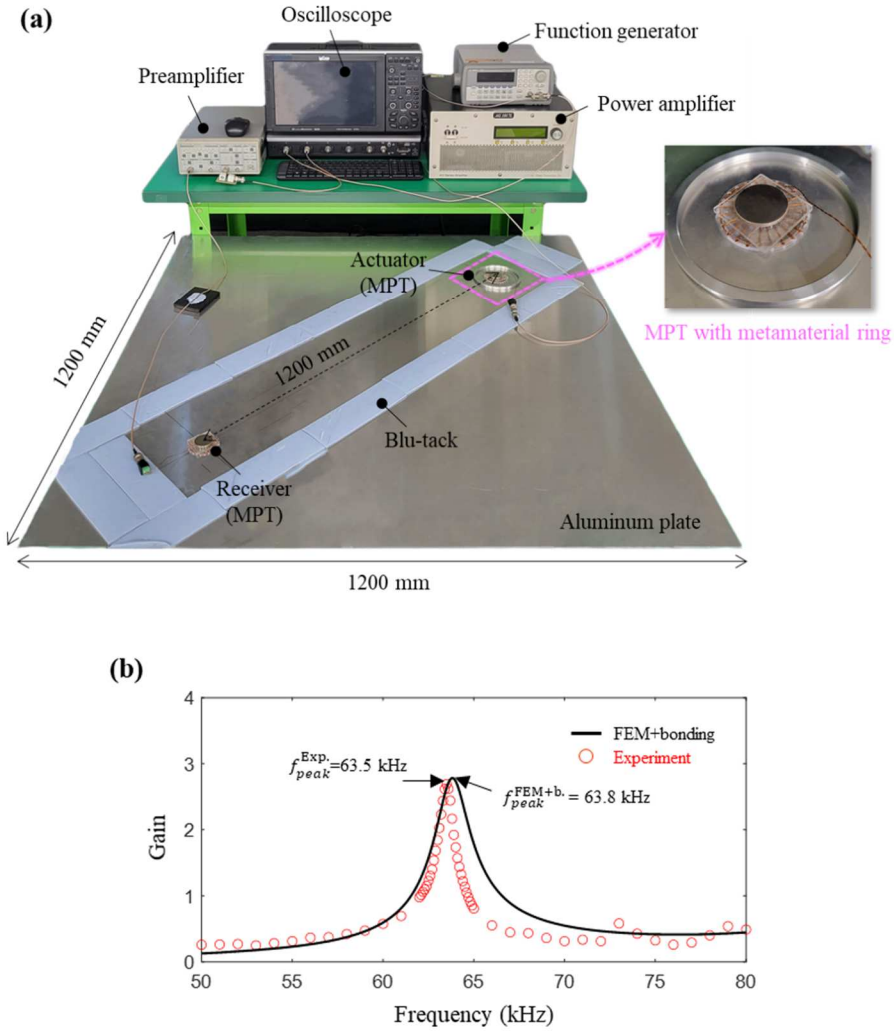

Fig. 3.11 Experimental demonstration in a thin plate. (a) Setup for experiments with a prototype of the meta-ring. A circular MPT is used to ensure the actuating and sensing of an omnidirectional SH wave. (b) A comparison of the FEM simulation considering the epoxy resin bonding layer (DP100, layer thickness = 0.2 mm) and experiment results for the enhancement gain $|H(\omega)|$ as a function of the frequency that denote the effect of the meta-ring on the radiated strain field $|S|$.

CHAPTER 4.
High gain elastic metamaterial superstrate for omnidirectional SH wave emission

4.1 Overview

As interest in nondestructive testing to examine the safety and reliability of the structure is growing, numerous studies on ultrasonic guided waves have been explored owing to their potential to propagate long distances from a single position in plates and shells[69-71]. Here, generating high intensity waves is the key issue to dominantly determine the performance, such as accuracy, inspection coverage, resolution, and power consumption. Moreover, whereas a unidirectional wave in which the intensity is kept constant in the propagation, obtaining a high gain for an omnidirectional wave, which covers a wide range of inspection easily and quickly but amplitude is innately decreased through the radiation, is much more emphasized. In this respect, the various design development of omnidirectional transducers to improve the gain of the waves has been suggested recently[1, 2]. Meanwhile, shear horizontal wave modes have several advantages in inspection, including a shorter

wavelength than their lamb wave mode counterparts (symmetric S and antisymmetric A) and less distortion and energy leakage from external causes such as fluids[10]. Particularly, fundamental shear mode (SH0) has unique nondispersive characteristics and propagates without mode conversion, making it an attractive option for such applications. Recent progress in omnidirectional transducers for shear horizontal wave generation has been made by utilizing the magnetostrictive phenomenon[13, 15-18], Lorentz force[14, 21, 22], and piezoelectric wafer[12, 22-27, 72], in response to these needs. Seung et al. developed the first SH wave magnetostrictive patch transducer(MPT) design to have an omnidirectionality with an annular nickel patch[15] and an electromagnetic acoustic transducer(EMAT) using a Lorentz force induced by a distinctive arrange of magnet with coil circuit[14]. After that, configuration optimization[15, 16] and phased array arrangement[17, 18] was further investigated. Piezoelectric transducers were relatively powerful compared to these two transducer models but suffered from an unequal intensity to the direction. Belanger and Bovin suggested a new piezoelectric transducer design with a six in-plane poled d_{15} mode PZT wafers to generate an omnidirectional SH wave[22]. Huan et al. proposed an enhanced omnidirectional SH wave transducer design by assembling twelve PZT elements composing the thickness-poled PZT ring[24]. In addition, the face shear d_{24} mode[12, 23], thickness poled d_{15} mode[25], and radially poled mode[27] of PZT elements were further developed to generate circumferential shear deformation yielding omnidirectional SH wave. However, the expected gains from these internal design improvements are limited, and complexity

renders them impractical.

As same as the high demand for transducers in elastics, developing high-gain antennas is a major challenge in the electromagnetic fields. Although phased array antennas have been proposed as a solution, they are known to increase system complexity and manufacturing costs. Fabry-Perot cavities have been suggested to achieve high-gain antennas as an alternative to the conventional approach[73, 74]. This simple design localizes sources between partially reflective surfaces (PRSs) and the ground, providing improved gains with a compact structure layout. Multiple reflections occur in the cavity, and when the transmitted waves match in phase under certain conditions, the emission is maximized with an increase in PRS reflectivity. With an elastic metamaterial, a similar concept to enhance the wave emission can also be applied. Metamaterials have been a topic of interest in recent years as artificially engineered structures that can achieve extreme characteristics for wave manipulation, such as negative density and bulk modulus[35, 36, 39, 40, 49, 75], negative shear modulus[34], and even anisotropic properties[50-53]. Lee et al. suggested a new unit cell design that breaks the intrinsic relationship between density and stiffness. By dividing the structure into two substructures, the effective mass, and stiffness of the elastic metamaterial were independently tuned[40]. Park et al. developed discrete continuum substructures separating the responses of dipolar and monopolar resonators through a deliberate transverse placement of the resonators. They show that the possibility to manipulate the mechanical properties in a completely decoupled manner[49]. Utilizing these metamaterials capable of

controlling wave properties may enable the design of mechanical PRS in elastics. Unfortunately, unlike electromagnetic fields that are freely designable in a wave propagating medium, designing in-plane metamaterials in elastic fields is unsuitable for non-destructive inspection as it requires processing test objects. Instead, out-of-plane metamaterials as types of pillars[76-79] and superstrate[47], which are separately fabricated and adhesive to the test structure, can be considered for practical applications. Yan et al. proposed surface-bonded elastic metamaterials consisting of lead discs with silicone rubber to manipulate an effective mass density profile that enabled the focusing of ultrasonic Lamb waves in an aluminum plate[76]. Wang et al. reported a single-phase double-sided pillared metamaterial capable of achieving both negative mass density and elastic modulus by adjusting the resonance mode of both pillars[77], and also developed a new mechanism involving the torsional resonance of stubs realizing negative effective shear modulus[78]. Tian et al. proposed a non-perforated resonant elastic metamaterial with complete mode converting capability from Lamb waves into shear horizontal waves[79]. Tian et al. proposed a superstrate design of elastic phased diffraction gratings for passive and multiple manipulations of Lamb and Rayleigh waves in solids[47]. They show that superstrate can modulate the waveguide's effective thickness and composition, yielding changes in dispersion. Nonetheless, the previous studies have required a large design space for periodic arrangements, and only to focus on the wavefront control of the one-dimensional propagation conditions. No direct method for controlling impedance has been proposed. Moreover, the physical features of

omnidirectional propagation problem have not been considered.

In this paper, we propose a novel elastic metamaterial superstrate that can significantly enhance the emission of omnidirectional shear horizontal waves. The elastic metamaterial superstrate is an easy-to-design structure, forming a Fabry-Perot cavity inside by locally increasing impedance. To interpret the mechanical principle of the emission enhancement phenomenon, we use an effective medium model substituting the superstrate structure. Our theoretical foundation demonstrates that two necessary conditions related to the geometry of the structure activate the Fabry-Perot resonance cavities. Additionally, we can attain the maximum gain up to the increased impedance ratio through the metamaterial. Superstrate design, corresponding to the theoretical model, is contrived based on the unique nondispersive characteristics of the SH0 wave mode. The thickness of the superstrate structure adjusts the varying impedance, achieving specific desired effective properties in a straightforward manner. Furthermore, our proposal operates independently, enabling high gain enhancement through multiple superpositions.

Compared to another type that relies on resonators[67, 68, 80] consisting of a discrete mass-spring model, our superstrate structure features the impedance selection only to be determined by the thickness. Specifically, in previous research by the authors, a resonant structure, meta-ring, was proposed for SH wave emission efficiency enhancement[80]. However, our new design is analyzed in a distinctly different approach, resulting in an explicit design and gain determination. In addition, as a small number of cycles ultrasonic signal is utilized in non-destructive tests, our

proposed superstrate model outperformed the resonator model in the minimum necessity cycles. The harmonic simulation results support the theoretical model analyzing the mechanical behavior of our proposed superstrate metamaterial. Afterward, transient analysis of numerical simulation and experiments are carried out to evaluate the performance and effectiveness of the emission enhancement.

4.2 Theoretical analysis

Fig. 4.1 shows a schematic illustration of the emission enhancement for omnidirectional shear horizontal waves that we intend to realize with our elastic metamaterial superstrate arrangement. In this research, the complicated omnidirectional propagation problem can be simplified to a radial one-dimensional propagation problem with axis-symmetry, as addressed in our previous work[80]. We aim here to investigate the theoretical background on wave emission enhancement phenomenon so that the effective medium model is used to substitute the effect of the elastic metamaterial superstrate. And, we first establish the matrix form of the omnidirectional wave propagation in cylindrical coordinates. Based on the matrix form, we interpret the wave emission enhancement phenomenon using a method of transfer matrix and scattering parameters that have never been proposed in the omnidirectional propagating problem. We then extend the theoretical interpretation from single to multi-layer to explore the possibility of near-infinite amplification.

4.2.1 Transfer matrix and scattering parameter with the effective medium

Now, we analyze the emission enhancement phenomenon of the elastic metamaterial superstrate substituted by the effective medium using the matrix form in Section 2.3. Considering the analytical model as shown in Fig. 4.2(a), the wave field in each medium can be described with mechanical characteristic parameters for the base plate given k_0 and z_0, and variables of the effective medium consisting of k_m and z_m. Under these conditions, we will describe the magnitude of the transmitted wave if the omnidirectional shear horizontal wave generated from the source with $F_{act}e^{i\omega t}$ passes through the effective medium with a width of d located at the radial position W.

Firstly, we need to examine the relation between the magnitude of actuating source, and the amplitude of the wave propagated through the test plate at the point $r = a$. Using the displacement continuity and force equilibrium condition, we can obtain

$$\begin{bmatrix} u_\theta \\ \sigma_{r\theta} \end{bmatrix} = Z(k_0, z_0)H(k_0, r)\begin{bmatrix} A_1 \\ B_1 \end{bmatrix}, \quad (r < a) \tag{4.1a}$$

$$\begin{bmatrix} u_\theta \\ \sigma_{r\theta} \end{bmatrix} = Z(k_0, z_0)H(k_0, r)\begin{bmatrix} A_2 \\ B_2 \end{bmatrix}, \quad (a < r \le W) \tag{4.1b}$$

$$\begin{bmatrix} u_\theta \\ \sigma_{r\theta} \end{bmatrix}_{r=a^+} - \begin{bmatrix} u_\theta \\ \sigma_{r\theta} \end{bmatrix}_{r=a^-} = \begin{bmatrix} 0 \\ F_{act} \end{bmatrix} \tag{4.2}$$

where A_1, B_1, A_2, and B_2 denote the coefficient of waves propagating outward and inward in Medium 1 and 2, respectively. Meanwhile, in Medium 1, the axis-symmetry condition leads the coefficient A_1 and B_1 to be the same. Then, Eqs. (4.1a, b) and (4.2) are combined as

$$\begin{bmatrix} A_2 \\ B_2 \end{bmatrix} = H(k_0, a)^{-1} \begin{bmatrix} 2A_1 J_1(ka) \\ -\dfrac{F_{act}}{z_0 \omega k} + 2A_1 J_2(ka) \end{bmatrix} \tag{4.3}$$

Now, we use a transfer matrix defined in cylindrical coordinates to analyze omnidirectional propagating waves. In Medium 3, the transfer matrix representing a relationship of wave motion between the point $r = W$ and $r = W + d$ is defined as

$$\begin{bmatrix} u_\theta \\ \sigma_{r\theta} \end{bmatrix}_{r=W+d^-} = T \begin{bmatrix} u_\theta \\ \sigma_{r\theta} \end{bmatrix}_{r=W^+} \tag{4.4}$$

However, the matrix form of the wave motion in Medium 3 can be expressed in

$$\begin{bmatrix} u_\theta \\ \sigma_{r\theta} \end{bmatrix} = Z(k_m, z_m) H(k_m, r) \begin{bmatrix} A_m \\ B_m \end{bmatrix}, \quad (W \le r \le W + d) \tag{4.5}$$

where A_m, B_m, k_m, and z_m denote the coefficient of waves propagating outward and inward, wavenumber, and impedance in Effective Medium, respectively. Substituting Eq. (4.5) into Eq. (4.4), the transfer matrix T between left boundary at $r = W$ and right boundary at $r = W + d$ of Effective Medium is defined as

$$T = Z(k_m, z_m)H(k_m, W+d)H(k_m, W)^{-1}Z(k_m, z_m)^{-1} \tag{4.6}$$

Moreover, the boundary conditions between two dissimilar medium at $r = W$ and $r = W + d$ lead following displacement continuity and force equilibrium

$$\begin{bmatrix} u_\theta \\ \sigma_{r\theta} \end{bmatrix}_{r=W^-} = \begin{bmatrix} u_\theta \\ \sigma_{r\theta} \end{bmatrix}_{r=W^+} \tag{4.7a}$$

$$\begin{bmatrix} u_\theta \\ \sigma_{r\theta} \end{bmatrix}_{r=W+d^-} = \begin{bmatrix} u_\theta \\ \sigma_{r\theta} \end{bmatrix}_{r=W+d^+} \tag{4.7b}$$

with

$$\begin{bmatrix} u_\theta \\ \sigma_{r\theta} \end{bmatrix} = Z(k_0, z_0)H(k_0, r)\begin{bmatrix} C_1 \\ C_2 \end{bmatrix}, \quad (W + d \le r) \tag{4.8}$$

where C_1 and C_2 denote the coefficient of waves propagating outward and inward in Medium 3, respectively. Substituting the Eqs. (4.1b), (4.5) and (4.8) into the Eqs. (4.7a, b), we can get the relationship between the coefficients of incident, reflected, and transmitted waves

$$\begin{bmatrix} C_1 \\ C_2 \end{bmatrix} = S\begin{bmatrix} A_2 \\ B_2 \end{bmatrix} \tag{4.9}$$

and the scattering matrix S is defined as

$$S = H(k_0, W+d)^{-1}Z(k_0, z_0)^{-1}TZ(k_0, z_0)H(k_0, W) \tag{4.10}$$

Using the relation between the magnitude of the actuating force and the amplitude of generated wave given in Eq. (4.3) with Eqs. (4.9) and (4.10), we can derive the coefficients in the resultant wave field in Medium 3 affected by the Effective Medium:

$$\begin{bmatrix} C_1 \\ C_2 \end{bmatrix} = SH(k_o, a)^{-1} \begin{bmatrix} 2A_1 J_1(ka) \\ -\dfrac{F_{act}}{z_0 \omega k} + 2A_1 J_1(ka) \end{bmatrix} \tag{4.11}$$

If there is no other dissimilar medium in $r > W + d$, no reflection exist in Medium 3 so that the component C_2 should be zero. Therefore, we can calculate C_1 / F_{act}, which denotes the amplified amplitude of the wave relative to the magnitude of actuating force, by solving Eq. (4.11). Next, we need to compare the result to the nominal case without an arrangement of the Effective Medium to assess the emission enhancement. Considering the Effective Medium same as the base plate, the scattering matrix S becomes 2×2 identity matrix I, and the ratio $C_{1,nom} / F_{act}$ can also be calculated with the same procedure. Then, the enhancement gain G is finally defined as

$$G = \frac{C_1}{C_{1,nom}} \tag{4.12}$$

4.2.2 Gain of emission enhancement by effective medium layer

To understand the mechanical mechanism behind the emission enhancement phenomenon of elastic metamaterial superstrate, we substitute it with the Effective Medium. However, the exact forms of the transfer matrix T and the scattering matrix S in Eqs. (4.6) and (4.10) contain complex matrix operations with Hankel functions, making it challenging to explicitly interpret the physical meaning of the

system. To reveal the underlying physics, we employ the asymptotic forms of the Hankel function by assuming $kW >> 1$ (as explained in Appendix A.2) as,

$$H_n^{(1)}(z) \approx \sqrt{\frac{2}{\pi z}} e^{i(z - \frac{n\pi}{2} - \frac{\pi}{4})} \tag{4.13a}$$

$$H_n^{(2)}(z) \approx \sqrt{\frac{2}{\pi z}} e^{-i(z - \frac{n\pi}{2} - \frac{\pi}{4})} \tag{4.13b}$$

where n denotes the order of Hankel function. Using these asymptotic forms, the relation in Section 4.2.1 can be rewritten. By substituting Eqs. (4.13a, b) into Eq. (4.6), the approximated form of transfer matrix T is expressed as

$$T = \begin{bmatrix} T_{11} & T_{12} \\ T_{21} & T_{22} \end{bmatrix} = \sqrt{\frac{W}{W+d}} \begin{bmatrix} \cos k_m d & \dfrac{\sin k_m d}{\omega z_m} \\ -\omega z_m \sin k_m d & \cos k_m d \end{bmatrix} \tag{4.14}$$

It is similar to that of the one-dimensional plane wave, but it clearly shows that the characteristics of an omnidirectional wave in which the amplitude decrease as it propagates. Also, by substituting Eqs. (4.13a, b) into Eq. (4.10) and combining with Eq.(4.14), the approximated form of scattering matrix S is expressed as

$$S = \begin{bmatrix} S_{11} & S_{12} \\ S_{21} & S_{22} \end{bmatrix} \tag{4.15a}$$

$$S_{11} = \frac{1}{2i}\left(2i \cos k_m d - (\frac{z_0}{z_m} + \frac{z_m}{z_0}) \sin k_m d \right) e^{-ik_0 d} \tag{4.15b}$$

$$S_{12} = \frac{1}{2}(-\frac{z_0}{z_m} + \frac{z_m}{z_0}) \sin k_m d \, e^{-ik_0(2W+d)} e^{-ik_0 d} \tag{4.15c}$$

$$S_{21} = \frac{1}{2}(-\frac{z_0}{z_m} + \frac{z_m}{z_0}) \sin k_m d \, e^{ik_0(2W+d)} e^{-ik_0 d} \tag{4.15d}$$

$$S_{22} = \frac{1}{2i}\left(2i\cos k_m d + (\frac{z_0}{z_m} + \frac{z_m}{z_0})\sin k_m d \right) e^{ik_0 d} \tag{4.15e}$$

On the other hand, we can unfold Eq. (4.3) and rewrite it as

$$\begin{bmatrix} A_2 \\ B_2 \end{bmatrix} = \frac{1}{\det H(k_0, a)} \begin{bmatrix} 2H_2^{(2)}(ka)A_1 J_1(ka) + H_1^{(2)}(ka) f - 2H_1^{(2)}(ka)A_1 J_2 \\ -2H_2^{(1)}(ka)A_1 J_1(ka) - H_1^{(1)}(ka) f + 2H_1^{(1)}(ka)A_1 J_2 \end{bmatrix} \tag{4.16}$$

where

$$f = \frac{F_{act}}{z_0 \omega k} \tag{4.17}$$

Here, the resultant expression of f can be obtained by substituting Eq. (4.15) into the Eq. (4.11) with the condition $C_2 = 0$ as

$$\begin{aligned} f &= \frac{-2A_1}{S_{21}H_1^{(2)}(ka) - S_{22}H_1^{(1)}(ka)} \\ &\times (J_1(ka)(S_{21}H_2^{(2)}(ka) - S_{22}H_2^{(1)}(ka)) + J_2(ka)(-S_{21}H_1^{(2)}(ka) + S_{22}H_1^{(1)}(ka))) \end{aligned} \tag{4.18}$$

Then, substituting Eq. (4.18) into Eq. (4.16) leads the expression of coefficient C_1, given by

$$C_1 = \frac{-2A_1 J_1(ka)}{S_{21}H_1^{(2)} - S_{22}H_1^{(1)}} \det S \tag{4.19}$$

We can confirm that the relation of $\det S = 1$ is also valid with Eq. (4.15). Thus, the solution of the ratio C_1 / f is derived as

$$\frac{C_I}{f} = \frac{1}{(S_{21}H_2^{(2)}(ka) - S_{22}H_2^{(1)}(ka)) + (-S_{21}H_1^{(2)}(ka) + S_{22}H_1^{(1)}(ka)) \times \frac{J_2(ka)}{J_1(ka)}} \tag{4.20}$$

In the nominal case without the Effective Medium exist, the scattering matrix S

becomes identity matrix so that the components are $S_{21}=0$ and $S_{22}=1$. Then, the ratio $C_{1,nom}/f$ is derived as

$$\frac{C_{I,nom}}{f}=\frac{J_1(ka)}{-H_2^{(1)}(ka)\times J_1(ka)+H_1^{(1)}(ka))\times J_2(ka)} \tag{4.21}$$

With Eqs. (4.20) and (4.21), the enhancement gain G is obtained

$$\begin{aligned} G &= \frac{1}{S_{21}+S_{22}} \\ &= \frac{2i}{e^{ikd}\left[2i\cos(k_m d)+\left[i(-\frac{z_0}{z_m}+\frac{z_m}{z_0})e^{ik(2_0W)}+(\frac{z_0}{z_m}+\frac{z_m}{z_0})\right]\sin(k_m d)\right]} \end{aligned} \tag{4.22}$$

This result shows that we can expect the emission enhancement through the arrangement of effective medium with the necessity geometric parameters W and d, and effective properties k_m and z_m.

Considering the case that the effective property k_m is same with k_0, and the ratio of effective impedance z_r ($=\frac{z_m}{z_0}$) is only varied, the magnitude of emission enhancement derived in Eq. (4.22) is rewritten as

$$|G|=\frac{2}{|(A_{re}+iA_{im})|} \tag{4.23a}$$

$$A_{re}=(z_r+\frac{1}{z_r})-(z_r-\frac{1}{z_r})\sin(2k_0W))\sin(k_0d) \tag{4.23b}$$

$$A_{im}=2\cos(k_0d)+(z_r-\frac{1}{z_r})\cos(2k_0W)\sin(k_0d) \tag{4.23c}$$

To achieve the maximized $|G|$ under a condition $z_r > 1$, the following two Fabry-Perot resonance condition should be satisfied:

$$\sin(2k_0 W) = 1 \tag{4.24}$$

$$\sin(k_0 d) = \pm 1 \tag{4.25}$$

And, these solutions lead to the maximized $|G|$ as

$$\max|G| = z_r \tag{4.26}$$

when two geometric parameters are set to be

$$W = \frac{(4n+1)}{4k_0}\pi, \quad (n = 0,1,2,...) \tag{4.27}$$

$$d = \frac{(4m+1)\pi}{2k_0}, \quad \frac{(4m+3)\pi}{2k_0}, \quad (m = 0,1,2,...) \tag{4.28}$$

The solutions Eq. (4.24) and Eq. (4.25) yield the doubly Fabry-Perot resonance condition for an emission enhancement of omnidirectional shear horizontal wave through the effective medium representing an effect of elastic metamaterial superstrate. It should be noticed that the forms of solutions are similar to the Fabry-Perot condition commonly used in one-dimensional propagation plane waves but requires different phase variations. In addition, we can expect the maximum gain G of emission enhancement proportional to the impedance ratio z_r by installing a single layer of elastic metamaterial superstrate.

On the other hand, the realization of this emission enhancement effect is not limited to a single layer. In other words, we can expect cumulative emission improvements

by arranging multiple layers of effective media. Fig. 4.2(b) shows an expanded analytic model to an arrangement of multiple layers of an effective medium representing each elastic metamaterial superstrate. The nth layer effective medium consists of the effective wavenumber $k_{m,n}$ and impedance $z_{m,n}$, located from the left boundary $r = r_{n,L}$ to the right boundary $r = r_{n,R}$ given as

$$r_{n,L} = \sum_{i=1}^{n-1} W_i + d_i + W_n, \quad r_{n,R} = \sum_{i=1}^{n} W_i + d_i, \quad (n = 1, \cdots, N) \tag{4.29}$$

Using Eq. (4.15), we can describe a scattering matrix S^n of the nth layer as

$$S^n = \begin{bmatrix} S_{11}^n & S_{12}^n \\ S_{21}^n & S_{22}^n \end{bmatrix} \tag{4.30a}$$

with

$$S_{11}^n = \left(\cos k_{m,n} d_n - \frac{1}{2i} \left(\frac{z_0}{z_m} + \frac{z_{m,n}}{z_0} \right) \sin k_{m,n} d_n \right) e^{-ik_0 d_n} \tag{4.30b}$$

$$S_{12}^n = \frac{1}{2} \left(-\frac{z_0}{z_{m,n}} + \frac{z_{m,n}}{z_0} \right) \sin k_{m,n} d_n e^{-ik_0 (r_{n,L} + r_{n,R})} \tag{4.30c}$$

$$S_{21}^n = \frac{1}{2} \left(-\frac{z_0}{z_{m,n}} + \frac{z_{m,n}}{z_0} \right) \sin k_{m,n} d_n e^{ik_0 (r_{n,L} + r_{n,R})} \tag{4.30d}$$

$$S_{22}^n = \left(\cos k_{m,n} d_n + \frac{1}{2i} \left(\frac{z_0}{z_{m,n}} + \frac{z_{m,n}}{z_0} \right) \sin k_{m,n} d_n \right) e^{ik_0 d_n} \tag{4.30e}$$

denoting the relation of the outward and inward going wave component in the left and right side medium based on the nth layer effective medium. Using Eqs. (4.30 a-e), the relation between the Medium N+1 and N+2 in the Fig. 2(b) is denoted as

$$\begin{bmatrix} C_1 \\ C_2 \end{bmatrix} = S^N \begin{bmatrix} A_{N+1} \\ B_{N+1} \end{bmatrix} \tag{4.31}$$

therefore, the resultant wave field in Medium N+2 from the wave actuation can be obtained as

$$\begin{bmatrix} C_1 \\ C_2 \end{bmatrix} = R^N H(k_o, a)^{-1} \begin{bmatrix} 2A_1 J_1(ka) \\ -\dfrac{F_{trd}}{z_0 \omega k} + 2A_1 J_1(ka) \end{bmatrix} \tag{4.32}$$

where R^N denotes the resultant multiplication of the scattering matrices,

$$R^N = \prod_{i=1}^{N} S^i \tag{4.33}$$

From the result of Eq. (4.22), the gain G^N of emission enhancement by N multiple layers is given as

$$G^N = \frac{1}{R_{21}^N + R_{22}^N} \tag{4.34}$$

However, according to the inductive approaches, Eq. (4.33) can be decomposed with the Nth layer and $(N-1)$ multiple layers. We can define the following recursion formula on the gain G^N by using the relation of complex conjugation between the diagonal components of the scattering matrix S as

$$\frac{1}{G^N} = \frac{S_{21}^N}{\widetilde{G}^{N-1}} + \frac{S_{22}^N}{G^{N-1}} \tag{4.35}$$

From the results of analysis on the single layer in Eqs. (4.22-4.28), the maximum gain G^N of the emission enhancement by arranging N multiple layers with the

assumption of effective wavenumbers $k_{m,n}$ equal to k_0 is

$$\max G^N = z_{r,N} \cdots z_{r,1} \tag{4.36}$$

where

$$z_{r,n} = \frac{z_{m,n}}{z_0} \tag{4.37}$$

when the following two Fabry-Perot resonance conditions are satisfied for the design of nth layer,

$$\sin(2k_0 r_{n,L}) = 1 \tag{4.38}$$

$$\sin(k_0 d_n) = \pm 1 \tag{4.39}$$

The findings of our study suggest that by arranging multiple layers, it may be possible to achieve near-infinite amplification of omnidirectional shear horizontal wave emission. We have determined that the key requirement for this phenomenon is the appropriate geometry of each layer to form a Fabry-Perot cavity without any interference between the other layers, enabling independent utilization of the gain capacity. In our theoretical analysis, the assumptions made on the wavenumbers $k_{m,n} = k_0$ are a distinctive feature of our proposed elastic metamaterial superstrate, which will be addressed in section 4.3.

4.3 Design of the elastic metamaterial superstrate

In this section, we examine the frequency response of the elastic metamaterial

superstrate, which was analyzed using an effectively substituted medium in the previous section to achieve the emission enhancement phenomenon. We explore the characteristics of the analytic solutions that enable the realization of emission enhancement through appropriate geometries and effective properties. Additionally, we will discuss the design of the elastic metamaterial superstrate that corresponds to the theoretically explored effective medium. To further confirm the effectiveness of our approach, we perform numerical simulations using the proposed structure.

4.3.1 Characteristics of elastic metamaterial superstrate

Here, we suggest the method of the elastic metamaterial superstrate design fully representing an effective medium with the impedance only varying modeled in our theory. We exploit the unique wave characteristics of the SH0 mode, which is the only non-dispersive wave mode in the plate-like waveguides. Fig. 4.3(a) shows the phase velocity of each shear horizontal wave modes. We can confirm that the phase velocity of the SH0 mode is unchanged along the variance of frequency and thickness of the plate, which shows a non-dispersive characteristic. Therefore, the wavenumber does not change even if the thickness varies at a fixed frequency within a certain range of the frequency and the thickness of the plate (the two products are within a range of about 1.56 MHz·mm or less). In this frequency range, we contrive a novel elastic metamaterial superstrate that is easy to design.

Fig. 4.3(b) shows an outline of our metamaterial superstrate design. The proposed

elastic metamaterial superstrate has identical geometric parameters W and d as those of the effective medium in the analytical model. However, it also has a variable thickness t_s in the z-direction, which allows for changes in impedance without affecting the wavenumber. By affixing the designed elastic metamaterial superstrate, we are able to achieve localized changes in impedance. The impedance of the base plate z_0 is denoted as $t_p\sqrt{\rho_0 G_0}$, while the effective impedance z_m of the area where the superstrate is attached is represented as $t_{tot}\sqrt{\rho_0 G_0}$, which is calculated by adding the thickness of the base plate t_p and the thickness of the superstrate t_s. By following our design scheme, we are able to significantly increase the effective impedance; however, the maximum increase is limited by the thickness of the plate and the target frequency.

4.3.2 Analytic discussion of elastic metamaterial superstrate

The analytic discussion based on our model is carried out to determine the proper design condition, including geometries and effective properties. Fig. 4.4 (a) shows a frequency response on the effective medium model to achieve the gain maximized at the target frequency 70 kHz. The base test plate is given as an aluminum consisting of density $\rho_0 = 2700\,kgm^{-3}$, young's modulus $E = 70\,GPa$ and Poisson's ratio $\nu = 0.33$ with the thickness p_t =1 mm. Therefore, the shear modulus G_0 can be

calculated as $\frac{E}{2(1+\nu)\rho_0}$, so that the phase velocity $c_s = \sqrt{\frac{G_0}{\rho_0}}$ and the nominal impedance z_0 of SH0 mode are $c_s = 3122\,m/s$ and $z_0 = 8429.3\,kg\,s^{-1}$, respectively. For the wave generation, the position a of the actuating source is given as 15 mm. From Eqs. (4.27) and (4.28), we can get the geometric design solution sets for the target frequency 69.9 kHz, as given in Tables 1 and 2. At our desired frequency, we have chosen the geometric parameters W and d to be 50.2 mm and 11.2 mm, respectively, for the compact system. And, the effective impedance z_{eff} is set to be $3z_0$ for the discussion. With the selected geometric parameters and effective parameter, the frequency response of the gain by the arrangement of single effective medium layer as described in Eq. (4.23) is plotted. We can observe that the analytically approximated gain solution is maximized to about 229.7% at the target frequency of 69.9 kHz. This result coincides with our theoretical prediction, which denotes that the impedance ratio determines the maximum gain as defined in Eq. (4.26). Moreover, we also investigate two necessity Fabry-Perot conditions to achieve maximized gain. Figs. 4.4(b) and (c) show the conditions of Eqs. (4.24) and (4.25) are also satisfied so that two phase conditions, $\sin(k_0 d)$ and $\sin(2k_0 W)$, are 1 at the desired frequency.

We also investigate how changes to geometric parameters and effective impedance affect the gain. Fig. 5 shows a geometric effect on the gain of our proposed model. The analytic gain as functions of W and d with a fixed effective impedance

$z_m(=3z_0)$ is given in Fig. 4.5(a). It is possible to observe a periodic solution set line that is relatively sensitive to the variable W and insensitive to the variable d. And examining the phase conditions of the geometric parameters on the sine function field offers a distinct understanding of the underlying physical implications, as shown in Fig. 4.5(b). The anticipated amplification increases consistently as the first phase condition, $\sin(2k_0W)$, for variable W approaches 1, while the second phase condition, $\sin(k_0d)$, for variable d, has two directions that increase as it approaches +1 and -1. Alternatively, considering the impact of the alteration in effective impedance, we can detect another effect on the amplification analyzed in Eq. (4.26). Fig. 3.6 shows the frequency response variation of the gain under fixed geometric conditions while only the ratio of the effective impedance to the nominal impedance is altered. By maintaining identical geometric parameters, the maximum gain can be achieved at the same target frequency. And the maximum gain is amplified by 199.9%, 299.7%, and 398.6% by setting the impedance ratio z_r to 2, 3, and 4, respectively, which is the same result as Eq. (4.26). These results conclude that it is analytically possible to increase the gain of emission enhancement by just increasing the effective impedance.

4.4 Numerical simulation of the emission enhancement

To verify the analytical model of the effective medium layer and the structural design

of an elastic metamaterial superstrate, we perform the numerical simulations using COMSOL Multiphysics 5.3. In the numerical simulation, we create a Finite Element Method (FEM) model with identical geometry conditions to the analytical model. Based on the design outlined in Section 4.3.2, the elastic metamaterial superstrate is made of aluminum, the same material as the test plate, and is implemented as a hollow cylinder-type structure with an inner diameter of W, a width of d, and a height of t_s. However, since the omnidirectional shear horizontal wave exhibits axisymmetric behavior, we conduct a wave analysis of the 2D axisymmetric partial pie-shaped model with asymmetric boundary conditions to reduce the computational cost. The numerical verifications are conducted to address two aspects: 1) verifying the effectiveness of the proposed elastic metamaterial superstrate and its agreement with the theory through harmonic simulation, and 2) testing the dependence of the capacity on the periodicity of the input signal through transient analysis.

4.4.1 Harmonic analysis

Fig. 3.7 depicts the gain $|G|$ of displacement amplification as a function of input frequency by an elastic metamaterial superstrate designed with FEM model in the harmonic condition. ere, each Figs. 3.7(a), (b), and (c) denote the results of the superstrate thickness t_s of 2 mm, 3 mm, and 4 mm, respectively, to denote the ratio z_r of the effective impedance to the normal impedance corresponds to 2, 3, and 4

since the thickness p_t of the plate is 1 mm. The displacement field plots are provided at the peak frequency to help comprehend the wave emission enhancement phenomenon of the elastic metamaterial superstrate. For the numerical simulation in the harmonic condition, the outermost region has been given a PML(perfectly matched layer) condition in order to fully confirm the effect of the metamaterial without considering the influence of the reflected wave. The numerical simulation results demonstrate a frequency response similar to the theoretical predictions and indicate that a maximum gain $|G|$ proportional to the impedance ratio can be achieved. This outcome provides evidence that the elastic metamaterial superstrate designed in the FEM model is implemented as intended in the theoretical model and exhibits the expected wave emission enhancement effect. And, examining the displacement field plot of the FEM model at the peak frequency f_{peak}^{FEM} of 68.5 kHz in numerical simulation, it becomes apparent that the intensity of the emitted wave is higher with the metamaterial superstrate installation than without it and that this intensity proportionally increases with thickness t_s. The discussion above confirms that our theory and the proposed elastic metamaterial superstrate design can effectively explain and achieve the enhanced emission effect of omnidirectional shear horizontal waves.

4.4.2 Transient analysis

The analysis of the wave emission enhancement effect of the metamaterial superstrate, as previously confirmed through theoretical models and numerical simulations, was conducted under the condition of inputting waves with an infinite number of cycles and achieving a steady state throughout the entire system. To confirm the practical feasibility of the proposed metamaterial superstrate, it is necessary to assess the amplification effect on emitted waves under shorter input cycles. In this respect, we conduct the transient analysis of the FEM model with several cycles of wave signal inputted. We selected a thickness of the superstrate as 2 mm($t_s = 2p_t$) in transient analysis. With this selection, the ratio z_r of the effective impedance to the normal impedance is 3, potentially resulting in a signal amplification effect of up to 300%. Fig. 4.8 illustrates a comparison of the displacement magnitude over time t at a particular point outside the metamaterial superstrate, away from the excitation source, with and without the presence of a superstrate. Here, the amplification effect of the following cases is compared where a sinusoidal signal, $\sin(2\pi f_t t)\times(t < N / f_t)$, with N = 10, 20, and 30 cycles is, respectively, input. As a result, the metamaterial superstrate showed a signal amplification effect of 162%, 228%, and 298% for the input signal of each cycle. These imply that our designed metamaterial superstrate exhibits a remarkable enhancement of wave emission for short-period input signals with only 10 cycles. Additionally, it can achieve its full potential with more than 30 cycles of wave inputs.

The transient analysis allows us to verify that the proposed method is sufficient with only a small cycle of signal input until it reaches a harmonic condition where perfect performance is implemented in a simulation environment. The reason for this can be attributed to the distinct design features: 1) It can be compactly designed within around 3 wavelengths ($\lambda = 4.46cm$ at target frequency). 2) The wave experiences a locally increased impedance change as it propagates through the system, undergoing the effect of substitution with a different material of the same wave speed in the plane. Thus, achieving the FP resonance phenomenon with a relatively small number of input cycles is feasible.

4.5 Experimental validation

In this section, experimental validation on the emission enhancement capability of our elastic metamaterial superstrate is carried out. The experimental setup, illustrated in Fig. 3.9(a) , involves using an aluminum plate (A6061, 1600 mm$\times$900 mm) with a thickness p_t of 1mm was used as a waveguide. We install a wave transmitter and sensor at a distance of 800mm from each other along the horizontal centerline. Here, we utilize a magnetostrictive patch transducer(MPT) to generate and measure the shear horizontal waves that propagate uniformly in all directions[13]. For the MPT configuration, we use an annular nickel patch with an inner diameter of 24 mm and an outer diameter of 55 mm and place a circular permanent magnet on top to form a

magnetic field. The aluminum superstrate structure, evaluated in transient analysis, is fabricated by laser beam machining to the dimensions of W as 50.2 mm, d as 11.2 mm, and a thickness of t_s as 2mm. The structure is then installed around the actuating transducer, ensuring that the two centers match well. We use epoxy resin (DP-100) to attach the superstrate structure and MPTs to the plate and affix the dissipative material, Blu-tack, to the edge of the plate to prevent the reflected wave from the boundary interfering with the estimation.

The following experimental procedure is carried out for two cases: 1) without the structure installation and 2) with the structure installation. Referring to the analysis results of the transient simulation, we generate a 30-cycle sine wave voltage signal with a 100 mV peak-to-peak amplitude using a function generator (Agilent 33250A), which is then amplified (30%G) by a power amplifier (AG1017L) and sent to the transmitter MPT. Following a deformation in the nickel patch attached to the plate caused by the magnetostrictive effect, a shear horizontal wave that propagates omnidirectionally along the waveguide is generated. We measure the propagated wave signal using the receiver MPT and amplify it (1000 times) with a preamplifier (SR 560) before being input to the oscilloscope (LeCroy Waverunner 104MXI). To minimize noise, we stored averaged data of 500 samples. We measure at 0.5 kHz intervals within the 60 kHz to 75 kHz frequency range to analyze the frequency response of the structure. And the gain is obtained by dividing the peak-to-peak voltage amplitude of those two cases. The measurement results are compared with the theory and FEM simulation in Figure 3.9(b). It is observed that the installation

of the superstrate structure resulted in a 205.5% amplification of the amplitude of the emitted wave at the peak frequency of 68.5 kHz. Also, the gain spectrum of the superstrate structure at varying excitation frequencies was found to be in agreement with the tendency predicted by FEM simulation. Although it was predicted that attaching the superstrate structure with a thickness t_s of 3 mm could result in a gain of up to 300% based on theory and FEM simulations, the actual amplification effect observed was limited. This is attributed to the relatively large contact area between the plate and the structure($\sim \lambda / 4$), strengthening the damping effect of the epoxy layer. Although attenuation exists, the experiment confirmed the effectiveness of the proposed metamaterial superstrate in enhancing emission.

4.6 Summary

To enhance the emission power of the ultrasonic transducer, we propose a superstrate structure, a simple circular design with a high gain for the emission of omnidirectional shear waves. The superstrate structure is designed according to geometric conditions that can form Fabry-Perot cavities based on a theoretical model established using a transfer matrix and scattering matrix, which are modified and defined to fit the cylindrical coordinates. In addition, the amplification gain can be determined exactly by adjusting the thickness of the superstrate made of the same material as the target plate. As attaching the superstrate to the plate, only the

impedance of the bonded area is increased, whereas the phase speed and wave number inward are unchanged. It is due to the characteristics of a fundamental shear horizontal wave, which are the only non-dispersive among ultrasonic guided wave modes.

The performance of the proposed elastic metamaterial superstrate is evaluated by analytics, numerical simulations, and experiment. Once the superstrate with the target frequency of 70 kHz, determined by the radial geometric conditions, is bonded to the test plate, we confirmed that the amplification of the emitted wave amplitude exactly follows the impedance ratio increment modulated by the thickness and verified theoretical prediction through the harmonic analysis of numerical simulation. Moreover, the performance of the superstrate structure is affected by the number of cycles required for the formation of Fabry-Perot cavities. To assess its effectiveness, we conducted a transient analysis of the superstrate structure with an impedance ratio of 3. The results showed that even in a short signal of 10 cycles, it exhibited a significant amplification effect of 162% and perfect performance over 30 cycles. Also, our finding was validated by the experiment, which revealed that the attachment of the superstrate structure resulted in a significant amplification effect of 205.5% at the peak frequency. The proposed novel elastic metamaterial superstrate offers an innovative and compatible method for enhancing the emission of omnidirectional SH wave generated by any kinds of transducers, which could be useful for various purposes such as structural health monitoring (SHM) and nondestructive testing (NDT) in the future.

Table 4.1 The geometric design solutions of the variable W at the target frequency 70 kHz. (unit: mm)

	n = 0	***n = 1***	***n = 2***	***n = 3***	***n = 4***	***n = 5***
W	5.6	27.9	50.2	72.6	94.9	117.2

Table 4.2 The geometric design solutions of the variable d at the target frequency 70 kHz. (unit: mm)

	m = 0		***m = 1***		***m = 2***	
	(4m+1)	*(4m+3)*	*(4m+1)*	*(4m+3)*	*(4m+1)*	*(4m+3)*
d	11.2	33.5	55.8	78.2	100.5	122.8

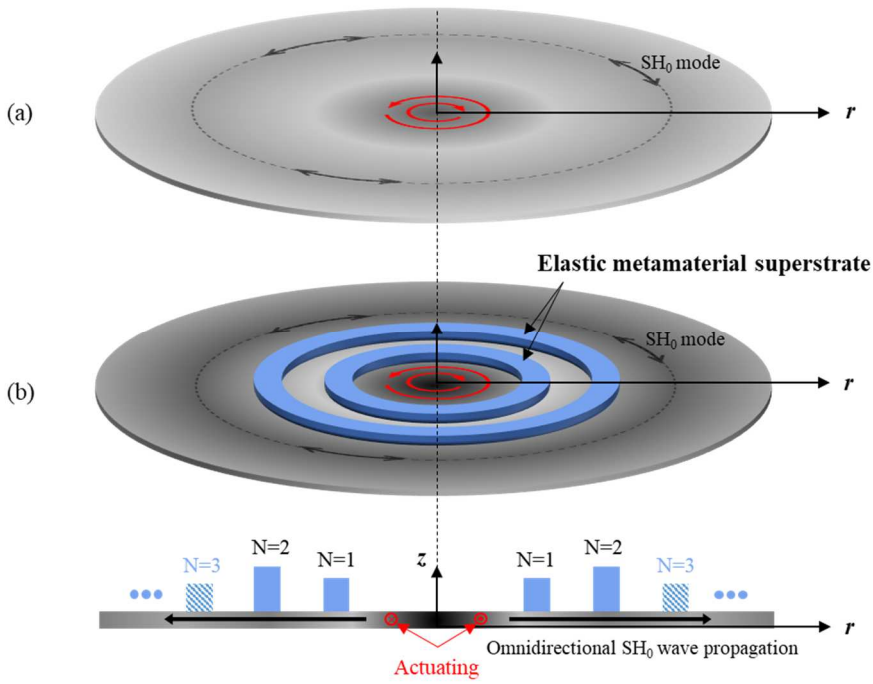

Fig. 4.1 Schematics of an elastic metamaterial superstrate enhancing an omnidirectional shear horizontal wave emission. (a) Propagation pattern of the waves generated from an excitation source on a thin plate structure. The amplitude of the wave expressed by the darkness of the color is decreased with the inverse square of the propagation distance. (b) Illustrations of an emission enhancement through the installation of the superstrate structure.

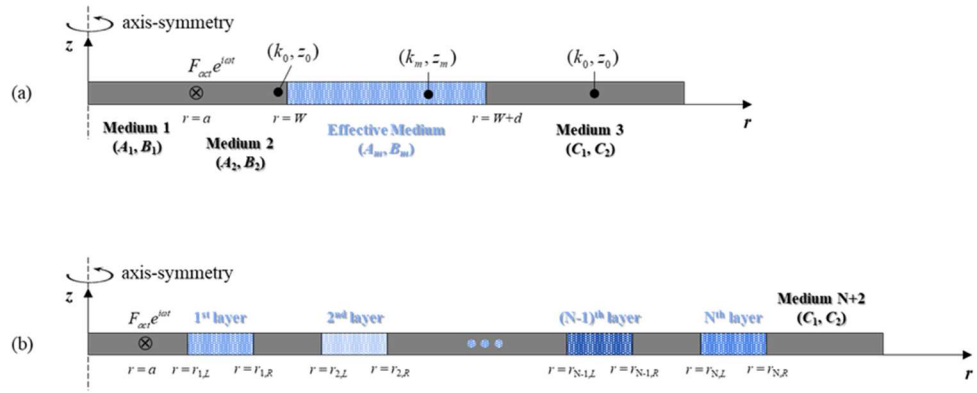

Fig. 4.2 Analytical model of (a) single layer and (b) multiple layers of an effective medium substituting an elastic metamaterial superstrates in an axis-symmetric one-dimensional propagation problem.

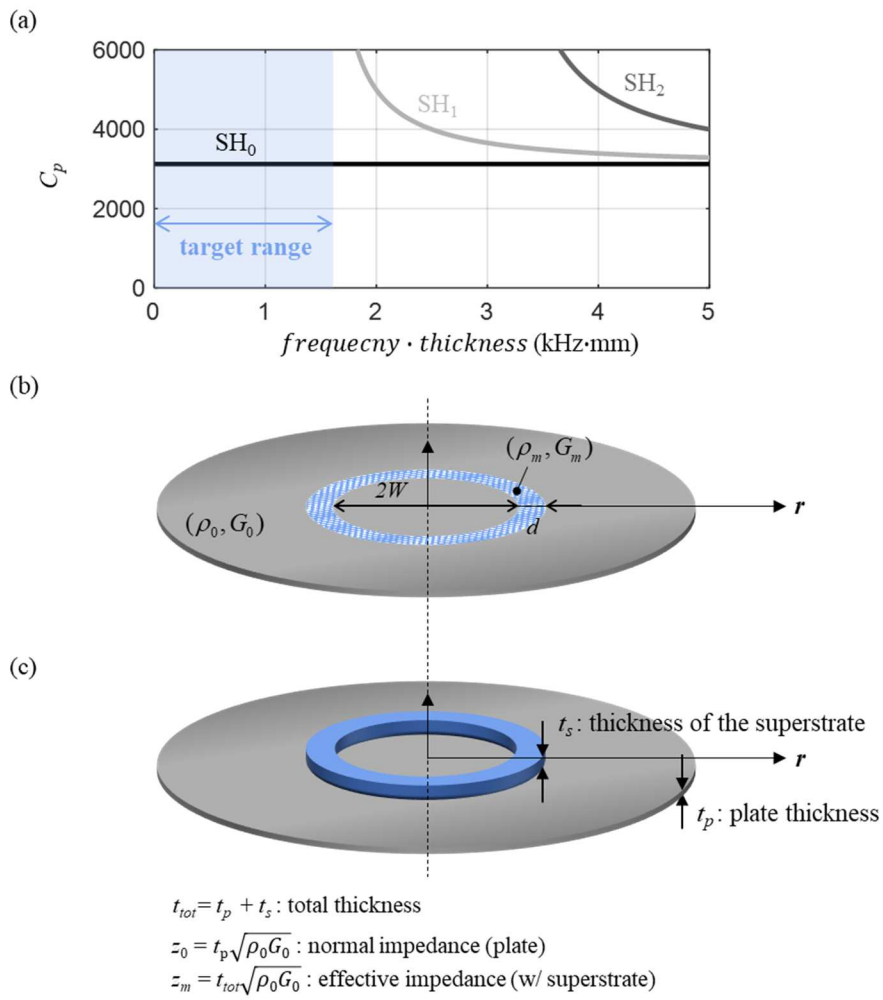

Fig. 4.3 (a) The phase velocity plot of the shear horizontal wave modes and the target frequency range interest. (b) Analytic concept of an effective medium consists of the geometric parameters W and d, and (c) realized structure of the elastic metamaterial superstrate design with the same geometric parameters and the newly added thickness variable t_s.

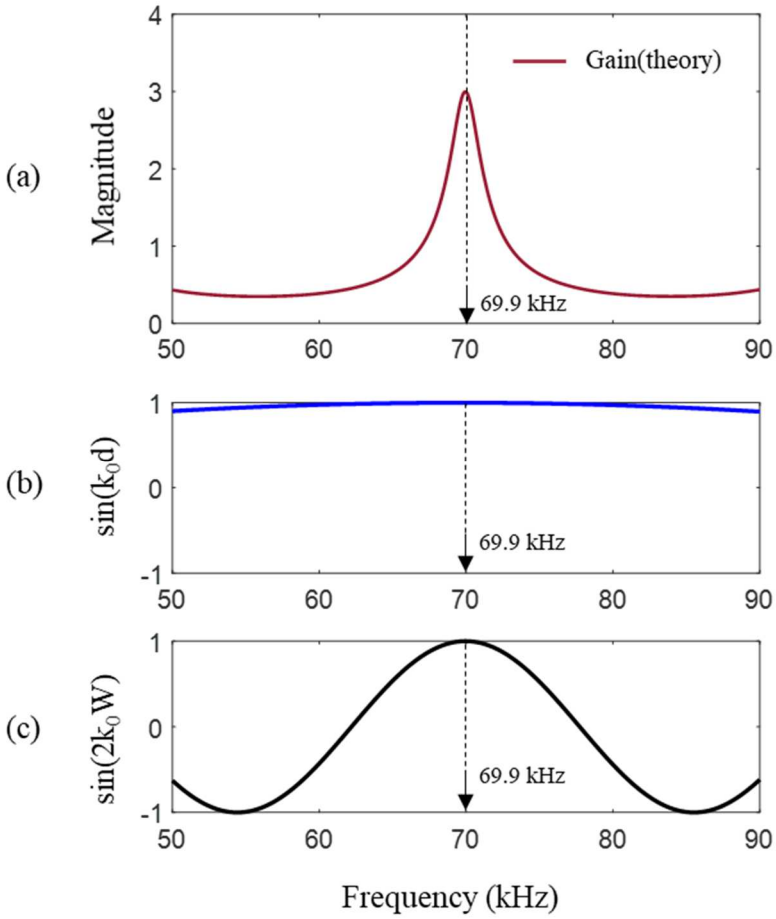

Fig. 4.4 Analytic solution of an emission enhancement (gain) and two Fabry-Perot conditions of the geometric parameters W and d of effective medium.

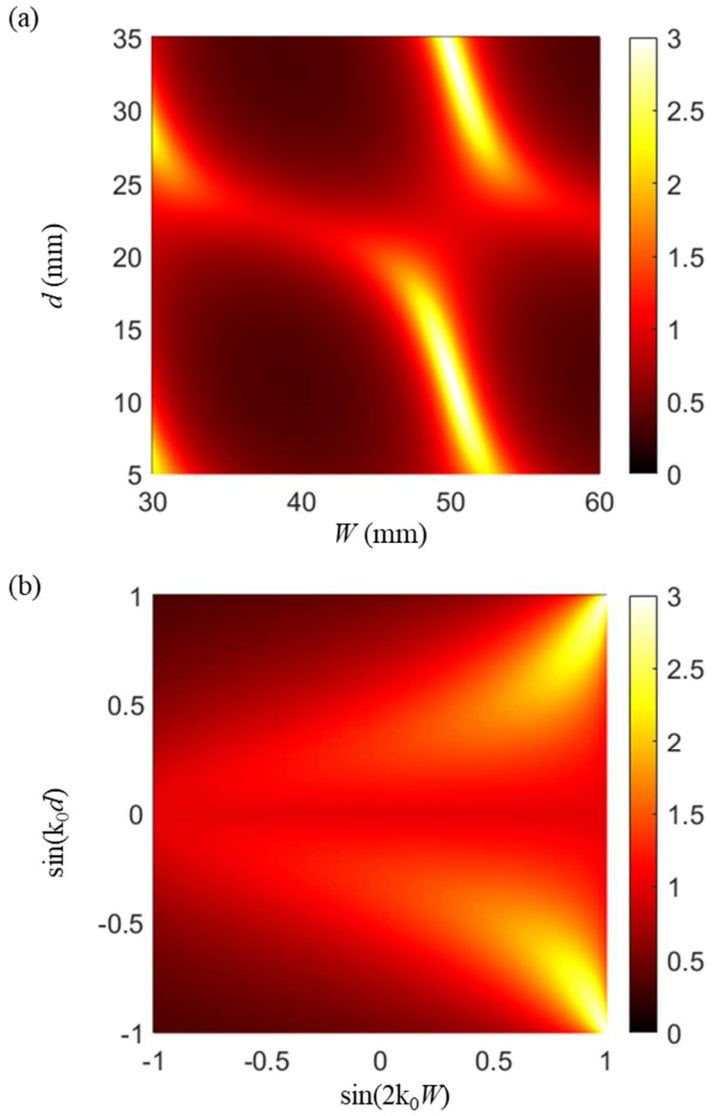

Fig. 4.5 (a)Analytical gain as functions of the geometric design parameters W and d of the effective medium. The impedance ratio z_r of the effective medium to the normal medium is set to 3, and the effective wavenumber is the same as that of the normal medium. (b) Plot of analytical gain converted to sine fields for each geometric variable

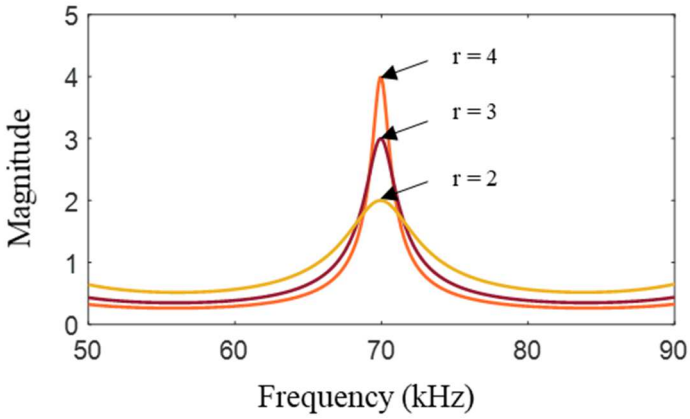

Fig. 4.6 Analytical model of (a) single layer and (b) multiple layers of an effective medium substituting an elastic metamaterial superstrates in an axis-symmetric one-dimensional propagation problem.

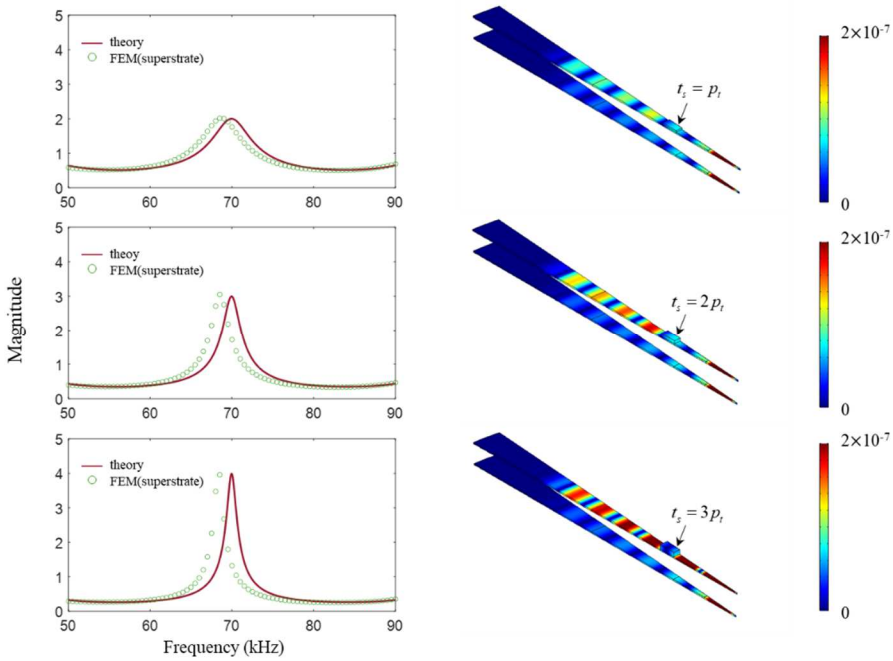

Fig. 4.7 Comparison the gain enhancement. Each results indicate FEM simulation of elastic metamaterial superstrate design and the theory with an effective medium. Gain as a function of frequency is plotted under a following condition; (a) impedance ratio $z_r = 2$, (b) impedance ratio $z_r = 3$, and (d) impedance ratio $z_r = 4$.

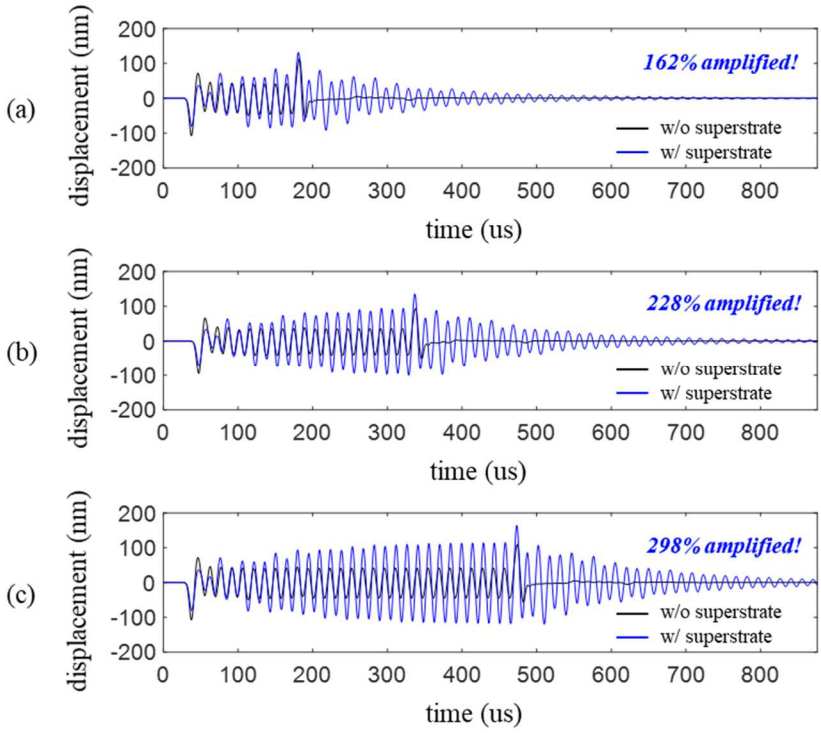

Fig. 4.8 Gain dependence on the input signal cycles. Transient analysis results of the input signal of (a) 10-cycles sinusoid, and (b) 20-cycles sinusoid, and (c) 30-cycles sinusoid without and with the elastic metamaterial superstrate.

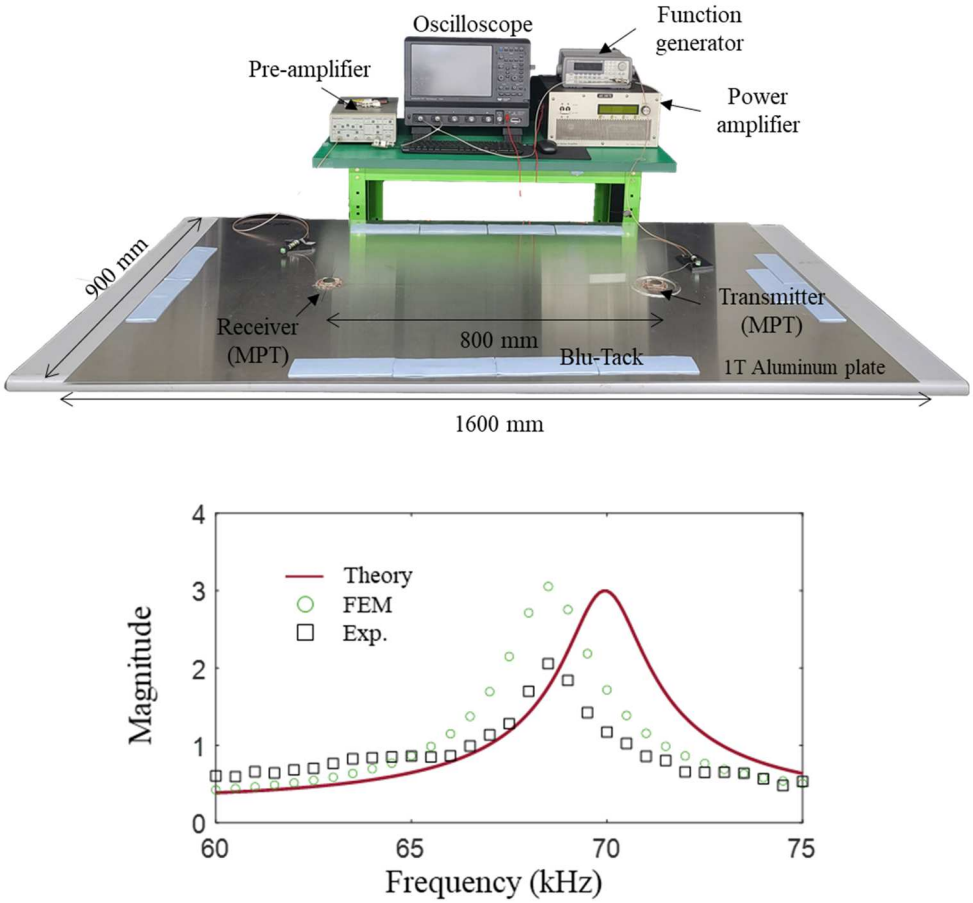

Fig. 4.9 The experimental setup and result data for validation. (a) Experimental setup with an illustration of the designed metamaterial superstrate installed on an aluminum plate around the transmitter. (b) The measured gain(squares) compared to that of theory(solid lines) and FEM(circles).

CHAPTER 5.
Conclusions

In this dissertation, elastic metamaterials, which improve the transduction efficiency of omnidirectional shear horizontal wave transducers in a nondestructive manner, were proposed. This method is independent and compatible with transducer types such as magnetostrictive patch transducer, electromagnetic-acoustic transducer, and piezoelectric transducer, providing additional gains for improvement through reconstruction for all types of transducers. To realize the unusual wave phenomenon, special metamaterials to be installed on a test plate or shell in a design space outside the transducer have been contrived. The common physical principles penetrating the two metamaterials are impedance and Fabry-Perot resonance. Both metamaterials share common physical principles of impedance and Fabry-Perot resonance. To clarify this relationship, rigorous analysis of each metamaterial, including the interpretation on mechanical mechanism, necessary design conditions, and practical effectiveness is conducted. The detailed investigation of this work can be summarized as follows.

First, the emission of the omnidirectional shear horizontal wave can be enhanced by employing a metamaterial ring designed based on the resonator structure. The mass and stiffness models allow us to interpret wave fields and responses by metamaterial ring based on resonance structure and to confirm the amplification of the output at a certain frequency. Furthermore, the physical meaning inherent here can be known by interpreting an equivalent system in which the metamaterial ring is replaced with an effective medium. Metamaterial ring reduces the effective impedance of the inside area where the transducer is installed, resulting in high amplitude displacement. Meanwhile, due to the impedance difference, the transmitted wave through the boundary decreases. However, forming a Fabry-Perot resonance cavity inside at the peak frequency through metamaterial ring can overcome this problem and highly enhance the wave emission. The design of the metamaterial ring is determined by two independent variables, its resonance frequency, and radius, which determine its performance and target frequency. The corresponding structure was designed using finite element analysis, and wave emission could be improved by installing the realized metamaterial ring structure. Numerical simulations and experiments have confirmed the validity and practicality of metamaterial rings for wave amplification phenomena.

Secondly, an elastic metamaterial superstrate with a non-resonant structure is proposed that can freely modulate the impedance of the local area and significantly improve the emission of omnidirectional shear horizontal waves. Metamaterial

superstrate is theoretically analyzed using transfer matrix and scattering matrix methods, which is useful for developing a general theory about the superposition of gains through multiple arrays. In elastic media, wave properties are generally described in terms of density and modulus. But instead, we define an effective medium with effective wavenumber and effective impedance derived from the two properties and investigate the physics of the specific wave phenomena caused. Using the scattering matrix method simplifies the quantitative analysis of waves transmitted through an effective medium. The superstrate structure is designed by two conditions independent of each other 1) geometry forming a Fabry-Perot resonance cavity, and 2) impedance determining the size of the emission improvement gain. The realized metamaterial superstrate is a simple annular-shaped structure consisting of radius, width, and height and can only change the impedance of the local region. The amplification phenomenon caused by superstrate could be confirmed through harmonic analysis using numerical simulation. In addition, the practical usefulness of the proposed metamaterial superstrate has been evaluated through transient analysis and experiments, and its effectiveness for emission enhancement effects has been demonstrated.

In conclusion, this dissertation suggested two types of elastic metamaterials to achieve a high-performance transducer system capable of enhancing the emission of omnidirectional shear horizontal waves. With their sophisticated theoretical analysis and design methods, the proposed elastic metamaterials are expected to provide an

innovative way to develop the omnidirectional transducer, having been far behind the unidirectional transducer. With the increasing importance of omnidirectional waves in nondestructive testing and ultrasonic imaging, these models have the potential to contribute to significant advancements in application performance.

APPENDIX A.
Validation of approximation in theoretical analysis

A.1 Background for far-field approximation for meta-ring

To confirm the satisfaction of the far-field approximation, we compare the exact form and approximated form of the Hankel function in the desired range of the parameter $z = kW$. (Because W_{eff} is frequency-dependent and $W_{eff} \approx W$, one can use kW instead of kW_{eff} without loss of generality.) Because the Hankel function is a complex number valued, we divide the 1st and the 2nd-order Hankel functions into real and imaginary parts for comparison. Figs. A1(a) and (b) show that they are in good agreement when the parameter z is more than 6. To determine the approximation condition accurately, we also calculated the relative errors in the magnitude and phase of the Hankel functions. They are plotted in Fig. A1(c). The relative errors are defined as follows:

$$\text{Magnitude error of } H_i^{(1)}(z) \text{ as } \frac{\left|H_{i,exact}^{(1)}(z)\right| - \left|H_{i,approx.}^{(1)}(z)\right|}{\left|H_{i,exact}^{(1)}(z)\right|} \times 100\,(\%)\text{ , } (i=1,2), \quad \text{(A.1)}$$

Phase error of $H_i^{(1)}(z)$ as $\dfrac{\phi\left(H_{i,exact}^{(1)}(z)\right)-\phi\left(H_{i,approx.}^{(1)}(z)\right)}{2\pi}\times 100(\%)$, (i=1,2), (A.2)

where $\phi(\bullet)$ denotes the phase of the complex number. When the parameter z is 7.32, we used W = 52mm at the target frequency of 69.9 kHz. In this instance, the relative errors in the magnitude and phase of Hankel functions are 0.3% and 1.7%, respectively, for the 1st-order Hankel function, and 0.8% and 4.0%, respectively, for the 2nd -order Hankel function. Accordingly, the use of the approximated forms of the Hankel functions may be justified for the present analytic analysis performed to predict the essential wave phenomena.

A.2 Validation of transfer matrix and scattering matrix approximation

We discuss the validity of the far-field assumption $kW >> 1$ to approximate the transfer matrix T in Eq.(4.14) and the scattering matrix S in Eq.(4.15). As already analyzed in Section 2, these approximated forms are transformed from the exact forms of Eqs. (4.6) and (4.10) by using the asymptotic form of the Hankel function. To evaluate this process, we compared the components of the exact and approximated forms at the frequency range of interest from 50 kHz to 90 kHz, including the target frequency of 70 kHz, based on a specified geometry condition W = 50.2 mm. (which leads to $kW \in [5.05, 9.09]$) Since each component is

composed of a complex form, it is divided into a real part and an imaginary part for comparison. Figs. (A2) and (A3) show the comparison of the components in the exact form and the approximated form of the transfer matrix and the scattering matrix, respectively. The results indicate that the real and imaginary parts of each component in two forms for T and S match well in the broad frequency domain. Therefore, it is reasonable to use the approximated forms of the transfer matrix and scattering matrix to elucidate the fundamental principles in our analysis.

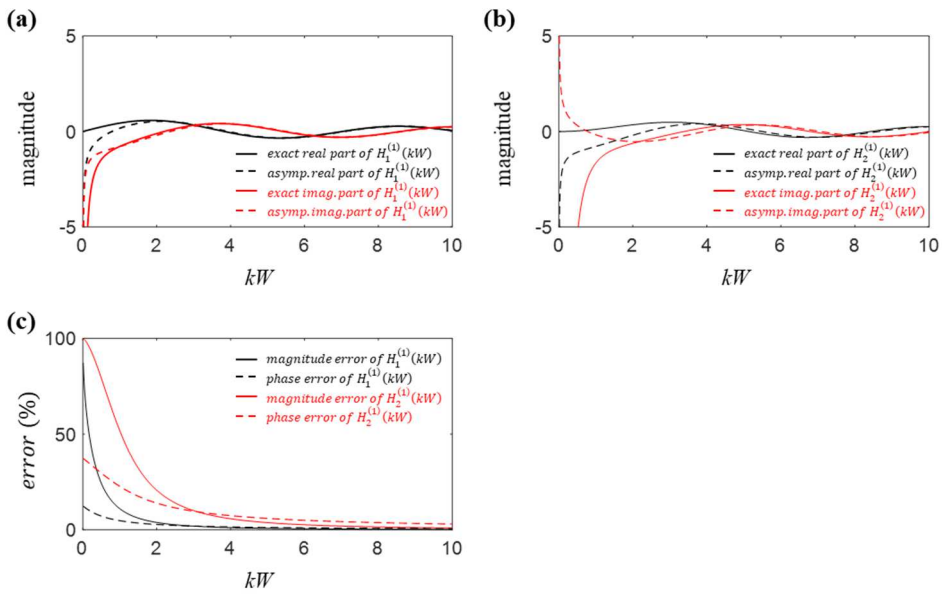

Fig. A.1 Background for far-field approximation for meta-ring. (a) Real and imaginary parts of the exact and asymptotic forms of 1st order Hankel function. (b) Real and imaginary parts of the exact and asymptotic forms of 2nd order Hankel function. (c) Error rates of the 1st and 2nd order Hankel functions in magnitude and phase.

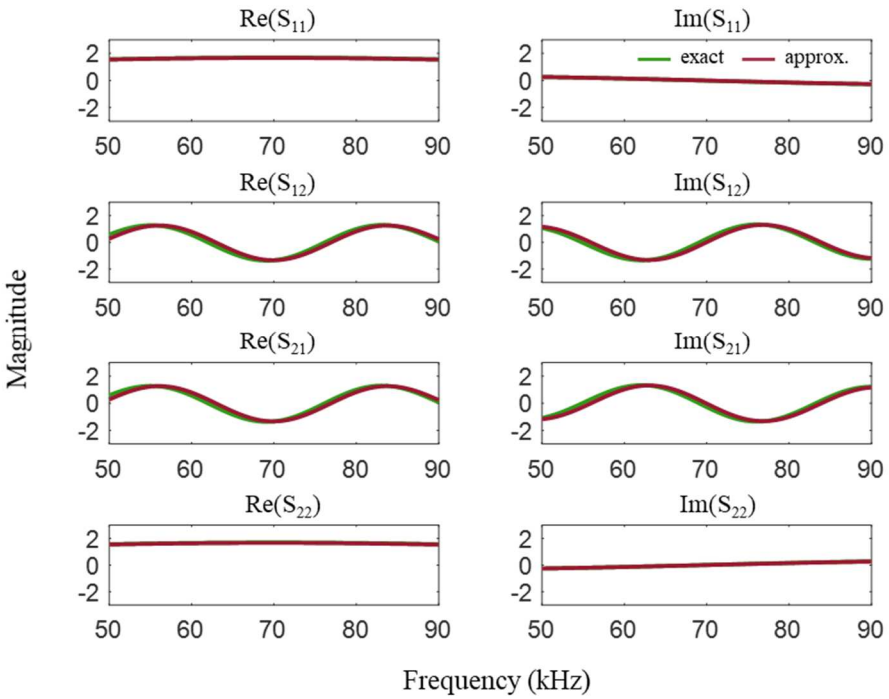

Fig. A.2 Comparison of the exact and approximated forms of scattering matrix S. Green and brown curves denote component of exact form and approximated form, respectively.

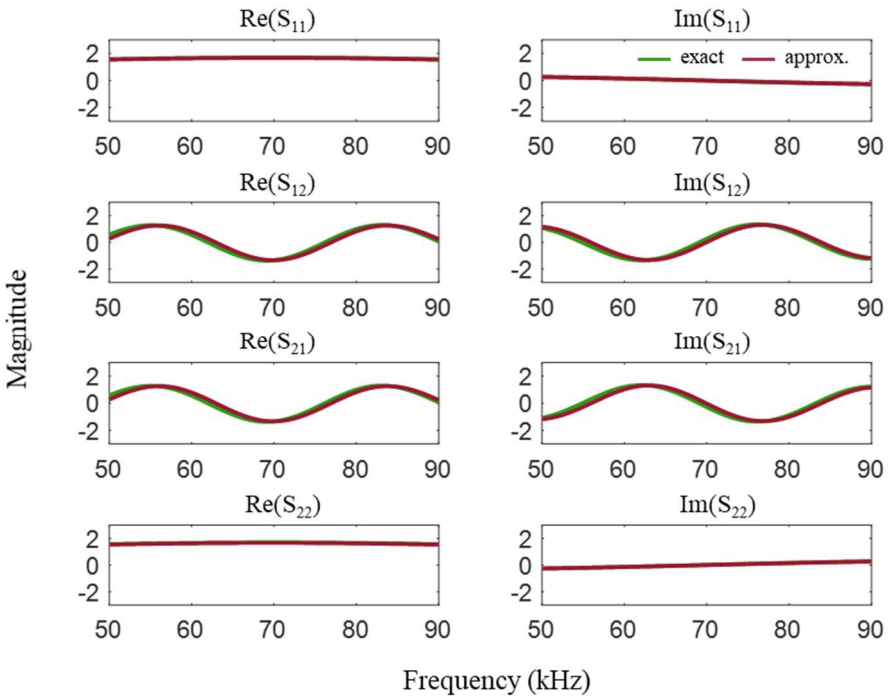

Fig. A.3 Comparison of the exact and approximated forms of scattering matrix S. Green and brown curves denote component of exact form and approximated form, respectively.

REFERENCES

[1] P.D. Wilcox, Omni-directional guided wave transducer arrays for the rapid inspection of large areas of plate structures, IEEE transactions on ultrasonics, ferroelectrics, and frequency control, 50 (2003) 699-709.

[2] P. Wilcox, M. Lowe, P. Cawley, Omnidirectional guided wave inspection of large metallic plate structures using an EMAT array, IEEE transactions on ultrasonics, ferroelectrics, and frequency control, 52 (2005) 653-665.

[3] J.P. Koduru, J.L. Rose, Transducer arrays for omnidirectional guided wave mode control in plate like structures, Smart Materials and Structures, 22 (2012) 015010.

[4] J.K. Lee, Y.Y. Kim, Tuned double-coil EMATs for omnidirectional symmetric mode lamb wave generation, Ndt & E International, 83 (2016) 38-47.

[5] P.D. Wilcox, M.J. Lowe, P. Cawley, The excitation and detection of Lamb waves with planar coil electromagnetic acoustic transducers, IEEE Transactions on ultrasonics, ferroelectrics, and frequency control, 52 (2005) 2370-2383.

[6] J.K. Lee, H.W. Kim, Y.Y. Kim, Omnidirectional Lamb waves by axisymmetrically-configured magnetostrictive patch transducer, IEEE transactions on ultrasonics, ferroelectrics, and frequency control, 60 (2013) 1928-1934.

[7] P. Huthwaite, R. Ribichini, P. Cawley, M.J. Lowe, Mode selection for corrosion detection in pipes and vessels via guided wave tomography, IEEE transactions on ultrasonics, ferroelectrics, and frequency control, 60 (2013) 1165-1177.

[8] W. Sun, G. Liu, H. Xia, Z. Xia, A modified design of the omnidirectional EMAT for antisymmetric Lamb wave generation, Sensors and Actuators A: Physical, 282

(2018) 251-258.

[9] J. Liu, S. Liu, C. Zhang, L. Jin, G. Zhao, A New Focused EMAT Design With Narrow Magnet to Achieve Both A0-Lamb Signal Enhancement and Waveform Distortion Correction, IEEE Sensors Journal, 22 (2022) 14786-14798.

[10] W. Zhou, H. Li, F.-G. Yuan, Guided wave generation, sensing and damage detection using in-plane shear piezoelectric wafers, Smart Materials and Structures, 23 (2013) 015014.

[11] H. Miao, S. Dong, F. Li, Excitation of fundamental shear horizontal wave by using face-shear (d36) piezoelectric ceramics, Journal of Applied Physics, 119 (2016) 174101.

[12] H. Miao, Q. Huan, F. Li, Excitation and reception of pure shear horizontal waves by using face-shear d24 mode piezoelectric wafers, Smart Materials and Structures, 25 (2016) 11LT01.

[13] H.M. Seung, H.W. Kim, Y.Y. Kim, Development of an omni-directional shear-horizontal wave magnetostrictive patch transducer for plates, Ultrasonics, 53 (2013) 1304-1308.

[14] H.M. Seung, C.I. Park, Y.Y. Kim, An omnidirectional shear-horizontal guided wave EMAT for a metallic plate, Ultrasonics, 69 (2016) 58-66.

[15] Z. Liu, X. Zhong, M. Xie, X. Liu, C. He, B. Wu, Damage imaging in composite plate by using double-turn coil omnidirectional shear-horizontal wave magnetostrictive patch transducer array, Advanced Composite Materials, 26 (2017) 67-78.

[16] J. Wu, Z. Tang, K. Yang, F. Lv, Signal strength enhancement of magnetostrictive patch transducers for guided wave inspection by magnetic circuit optimization, Applied Sciences, 9 (2019) 1477.

[17] Z. Liu, Y. Zhang, M. Xie, A. Li, W. Bin, C. He, A direction-tunable shear horizontal mode array magnetostrictive patch transducer, NDT & E International, 97 (2018) 20-31.

[18] C.I. Park, H.M. Seung, J.K. Lee, Y.Y. Kim, Analysis and design of an annular-array MPT for the efficient generation of omnidirectional shear-horizontal waves in plates, Smart Materials and Structures, 28 (2019) 075005.

[19] C.I. Park, H.M. Seung, Y.Y. Kim, Bi-annular shear-horizontal wave MPT tailored to generate the SH1 mode in a plate, Ultrasonics, 99 (2019) 105958.

[20] Z. Liu, Z. Huo, A. Li, C. He, B. Wu, Development of an omnidirectional SH 0 mode electromagnetic acoustic transducer employing a circumferential periodic permanent magnet array, IEEE Sensors Journal, 21 (2021) 7691-7701.

[21] Y. Zhang, W. Liu, N. Li, Z. Qian, B. Wang, D. Liu, X. Li, Design of a new type of omnidirectional shear-horizontal EMAT by the use of half-ring magnets and PCB technology, Ultrasonics, 115 (2021) 106465.

[22] P. Belanger, G. Boivin, Development of a low frequency omnidirectional piezoelectric shear horizontal wave transducer, Smart Materials and Structures, 25 (2016) 045024.

[23] H. Miao, Q. Huan, Q. Wang, F. Li, A new omnidirectional shear horizontal wave transducer using face-shear (d24) piezoelectric ring array, Ultrasonics, 74 (2017)

167-173.

[24] Q. Huan, H. Miao, F. Li, A uniform-sensitivity omnidirectional shear-horizontal (SH) wave transducer based on a thickness poled, thickness-shear (d15) piezoelectric ring, Smart Materials and Structures, 26 (2017) 08LT01.

[25] Q. Huan, H. Miao, F. Li, A variable-frequency structural health monitoring system based on omnidirectional shear horizontal wave piezoelectric transducers, Smart Materials and Structures, 27 (2018) 025008.

[26] Q. Huan, M. Chen, F. Li, A practical omni-directional SH wave transducer for structural health monitoring based on two thickness-poled piezoelectric half-rings, Ultrasonics, 94 (2019) 342-349.

[27] Q. Huan, M. Chen, A.-K. Soh, F. Li, Development of an omni-directional shear horizontal wave transducer based on a radially poled piezoelectric ring, Acta Mechanica Solida Sinica, 32 (2019) 29-39.

[28] C. Othmani, F. Takali, A. Njeh, Investigating and modeling of effect of piezoelectric material parameters on shear horizontal (SH) waves propagation in PZT-5H, PMN-0.33 PT and PMN-0.29 PT plates, Optik, 148 (2017) 63-75.

[29] C. Othmani, H. Zhang, C. Lü, F. Takali, Effects of initial stresses on the electromechanical coupling coefficient of SH wave propagation in multilayered PZT-5H structures, The European Physical Journal Plus, 134 (2019) 1-18.

[30] I.B. Salah, F. Takali, C. Othmani, A. Njeh, SH waves in a stressed piezoelectric semiconductor plates: Electron and hole drift phenomenon, International Journal of Mechanical Sciences, 223 (2022) 107281.

[31] S. Zhang, L. Yin, N. Fang, Focusing ultrasound with an acoustic metamaterial network, Physical review letters, 102 (2009) 194301.

[32] Z. Liang, J. Li, Extreme acoustic metamaterial by coiling up space, Physical review letters, 108 (2012) 114301.

[33] Y. Lai, Y. Wu, P. Sheng, Z.-Q. Zhang, Hybrid elastic solids, Nature materials, 10 (2011) 620-624.

[34] Y. Wu, Y. Lai, Z.-Q. Zhang, Elastic metamaterials with simultaneously negative effective shear modulus and mass density, Physical review letters, 107 (2011) 105506.

[35] X.-N. Liu, G.-K. Hu, G.-L. Huang, C.-T. Sun, An elastic metamaterial with simultaneously negative mass density and bulk modulus, Applied physics letters, 98 (2011) 251907.

[36] R. Zhu, X. Liu, G. Hu, C. Sun, G. Huang, Negative refraction of elastic waves at the deep-subwavelength scale in a single-phase metamaterial, Nature communications, 5 (2014) 5510.

[37] S.A. Cummer, J. Christensen, A. Alù, Controlling sound with acoustic metamaterials, Nature Reviews Materials, 1 (2016) 1-13.

[38] Z. Li, X. Wang, On the dynamic behaviour of a two-dimensional elastic metamaterial system, International Journal of Solids and Structures, 78 (2016) 174-181.

[39] J.H. Oh, H.M. Seung, Y.Y. Kim, Doubly negative isotropic elastic metamaterial for sub-wavelength focusing: Design and realization, Journal of Sound and Vibration,

410 (2017) 169-186.

[40] H. Lee, J.K. Lee, H.M. Seung, Y.Y. Kim, Mass-stiffness substructuring of an elastic metasurface for full transmission beam steering, Journal of the Mechanics and Physics of Solids, 112 (2018) 577-593.

[41] J. Zhao, H. Ye, K. Huang, Z.N. Chen, B. Li, C.-W. Qiu, Manipulation of acoustic focusing with an active and configurable planar metasurface transducer, Scientific Reports, 4 (2014) 6257.

[42] J. Chen, J. Xiao, D. Lisevych, A. Shakouri, Z. Fan, Deep-subwavelength control of acoustic waves in an ultra-compact metasurface lens, Nature communications, 9 (2018) 4920.

[43] S.-W. Fan, S.-D. Zhao, A.-L. Chen, Y.-F. Wang, B. Assouar, Y.-S. Wang, Tunable broadband reflective acoustic metasurface, Physical Review Applied, 11 (2019) 044038.

[44] S. Hur, H. Choi, G.H. Yoon, N.W. Kim, D.-G. Lee, Y.T. Kim, Planar ultrasonic transducer based on a metasurface piezoelectric ring array for subwavelength acoustic focusing in water, Scientific Reports, 12 (2022) 1485.

[45] S.W. Lee, J.H. Oh, Single-layer elastic metasurface with double negativity for anomalous refraction, Journal of Physics D: Applied Physics, 53 (2020) 265301.

[46] L. Cao, Z. Yang, Y. Xu, Steering elastic SH waves in an anomalous way by metasurface, Journal of Sound and Vibration, 418 (2018) 1-14.

[47] Z. Tian, L. Yu, Elastic phased diffraction gratings for manipulation of ultrasonic guided waves in solids, Physical Review Applied, 11 (2019) 024052.

https://doi.org/10.1103/PhysRevApplied.11.024052

[48] E. Bok, J.J. Park, H. Choi, C.K. Han, O.B. Wright, S.H. Lee, Metasurface for water-to-air sound transmission, Physical review letters, 120 (2018) 044302.

[49] C.I. Park, C. Piao, H. Lee, Y.Y. Kim, Elastic complementary meta-layer for ultrasound penetration through solid/liquid/gas barriers, International Journal of Mechanical Sciences, 206 (2021) 106619.

[50] J.M. Kweun, H.J. Lee, J.H. Oh, H.M. Seung, Y.Y. Kim, Transmodal Fabry-Pérot resonance: theory and realization with elastic metamaterials, Physical review letters, 118 (2017) 205901.

[51] X. Yang, J.M. Kweun, Y.Y. Kim, Theory for perfect transmodal Fabry-Perot interferometer, Scientific Reports, 8 (2018) 1-6.

[52] X. Yang, M. Kweun, Y.Y. Kim, Monolayer metamaterial for full mode-converting transmission of elastic waves, Applied Physics Letters, 115 (2019) 071901.

[53] J. Lee, M. Kweun, W. Lee, C.I. Park, Y.Y. Kim, Perfect transmission of elastic waves obliquely incident at solid–solid interfaces, Extreme Mechanics Letters, 51 (2022) 101606.

[54] E.M. Purcell, Spontaneous emission probabilities at radio frequencies, Confined Electrons and Photons: New Physics and Applications, (1995) 839-839.

[55] P. Goy, J. Raimond, M. Gross, S. Haroche, Observation of cavity-enhanced single-atom spontaneous emission, Physical review letters, 50 (1983) 1903.

[56] M. Noginov, H. Li, Y.A. Barnakov, D. Dryden, G. Nataraj, G. Zhu, C. Bonner,

M. Mayy, Z. Jacob, E. Narimanov, Controlling spontaneous emission with metamaterials, Optics letters, 35 (2010) 1863-1865.

[57] A. Poddubny, I. Iorsh, P. Belov, Y. Kivshar, Hyperbolic metamaterials, Nature photonics, 7 (2013) 948-957.

[58] A. Slobozhanyuk, A. Poddubny, A. Krasnok, P. Belov, Magnetic Purcell factor in wire metamaterials, Applied Physics Letters, 104 (2014) 161105.

[59] K. Song, S.-H. Lee, K. Kim, S. Hur, J. Kim, Emission enhancement of sound emitters using an acoustic metamaterial cavity, Scientific reports, 4 (2014) 4165.

[60] J. Zhao, L. Zhang, Y. Wu, Enhancing monochromatic multipole emission by a subwavelength enclosure of degenerate Mie resonances, The Journal of the Acoustical Society of America, 142 (2017) EL24-EL29.

[61] J. Zhao, R.A. Jahdali, L. Zhang, Y. Wu, Directional sound beam emission from a configurable compact multi-source system, Scientific reports, 8 (2018) 1018.

[62] M. Landi, J. Zhao, W.E. Prather, Y. Wu, L. Zhang, Acoustic Purcell effect for enhanced emission, Physical review letters, 120 (2018) 114301.

[63] F. Liu, W. Li, M. Ke, Rigorous analytical model for multipole emission enhancement using acoustic metamaterials, Physical Review Applied, 10 (2018) 054031.

[64] J. Mei, Y. Wu, Subwavelength acoustic monopole source emission enhancement through dual gratings, Scientific Reports, 9 (2019) 11659.

[65] Y. Lei, J.H. Wu, S. Yang, Broadband monopole emission enhancement using a dual acoustic grating, Physics Letters A, 408 (2021) 127486.

[66] M.K. Schmidt, L. Helt, C.G. Poulton, M. Steel, Elastic Purcell effect, Physical Review Letters, 121 (2018) 064301.

[67] K. Kim, C.I. Park, H. Lee, Y.Y. Kim, Near-zero effective impedance with finite phase velocity for sensing and actuation enhancement by resonator pairing, Nature Communications, 9 (2018) 5255.

[68] K. Kim, H.J. Lee, C.I. Park, H. Lee, Y.Y. Kim, Enhanced transduction of MPT for antisymmetric Lamb waves using a detuned resonator, Smart Materials and Structures, 28 (2019) 075035.

[69] A. Raghavan, C.E. Cesnik, Finite-dimensional piezoelectric transducer modeling for guided wave based structural health monitoring, Smart materials and structures, 14 (2005) 1448.

[70] V. Giurgiutiu, Tuned Lamb wave excitation and detection with piezoelectric wafer active sensors for structural health monitoring, Journal of intelligent material systems and structures, 16 (2005) 291-305.

[71] M. Mitra, S. Gopalakrishnan, Guided wave based structural health monitoring: A review, Smart Materials and Structures, 25 (2016) 053001.

[72] H. Miao, F. Li, Shear horizontal wave transducers for structural health monitoring and nondestructive testing: A review, Ultrasonics, 114 (2021) 106355.

[73] K. Konstantinidis, A.P. Feresidis, P.S. Hall, Multilayer partially reflective surfaces for broadband Fabry-Perot cavity antennas, IEEE Transactions on Antennas and Propagation, 62 (2014) 3474-3481.

[74] L. Zhang, X. Wan, S. Liu, J.Y. Yin, Q. Zhang, H.T. Wu, T.J. Cui, Realization of

low scattering for a high-gain Fabry–Perot antenna using coding metasurface, IEEE Transactions on Antennas and Propagation, 65 (2017) 3374-3383.

[75] Y. Ding, Z. Liu, C. Qiu, J. Shi, Metamaterial with simultaneously negative bulk modulus and mass density, Physical review letters, 99 (2007) 093904.

[76] X. Yan, R. Zhu, G. Huang, F.-G. Yuan, Focusing guided waves using surface bonded elastic metamaterials, Applied Physics Letters, 103 (2013) 121901.

[77] W. Wang, B. Bonello, B. Djafari-Rouhani, Y. Pennec, J. Zhao, Double-negative pillared elastic metamaterial, Physical Review Applied, 10 (2018) 064011.

[78] W. Wang, B. Bonello, B. Djafari-Rouhani, Y. Pennec, J. Zhao, Elastic stubbed metamaterial plate with torsional resonances, Ultrasonics, 106 (2020) 106142.

[79] Y. Tian, Y. Song, Y. Shen, Z. Yu, A metamaterial ultrasound mode convertor for complete transformation of Lamb waves into shear horizontal waves, Ultrasonics, 119 (2022) 106627.

[80] H.J. Kim, C.I. Park, K. Kim, Y.Y. Kim, Meta-ring for enhancing emission efficiency of omnidirectional SH waves, International Journal of Mechanical Sciences, 251 (2023) 108354.

ABSTRACT (KOREAN)

유효 임피던스 제어 탄성 메타물질을 이용한 전방향 전단 수평파 출력 증폭

김 홍 재
서울대학교 대학원
기계항공공학부

본 연구에서는 전방향 전파 전단 수평 파원의 출력을 크게 개선할 수 있는 실질적인 방법론에 대해 다루며, 이와 관련된 물리 이론을 정립하고 관련된 탄성 메타물질의 설계방법을 제시하는 것을 목표로 한다. 초음파의 세기는 검사 정확도와 직결되기 때문에, 초음파를 가진하는 트랜스듀서의 성능을 개선하려는 많은 방법들이 연구되어왔다. 특히, 넓은 검사범위를 효과적으로 대응할 수 있는 전방향 초음파 트랜스듀서는 고유의 물리적 특성으로 인해 전파방향으로 세기가 감소하여 그 필요성이 더욱 대두된다. 또한, 전단 수평파는 다른 초음파 모드에 비해 실직적인 유용성을 가짐에도 가진이 어려워 높은 세기를 확보하는데 어려움이 있다. 하지만, 기존의 연구들은 초음파를 생성하는 트랜스듀서의 내부적 설계에

국한되어 개발이 되어왔기에 실질적인 적용을 고려해보았을 때, 기대할 수 있는 세기는 한정된다.

본 연구에서는 내부적 설계와 무관하게 트랜스듀서 주위로 검사 대상체에 부착하는 비파괴적인 방법으로 초음파의 세기를 크게 증폭시킬 수 있는 메타물질을 제안한다. 먼저, 이산 질량과 스프링으로 구성된 공진기로 설계된 메타물질 링은 두 가지 물리 원칙 1) 낮은 임피던스 환경 조성과 2) 페브리-페로 공진 현상을 야기한다. 메타물질 링의 기계적 메커니즘과 유효 매질로 균질화된 등가 시스템을 해석함으로써 초음파의 방출 향상을 설명한다. 트랜스듀서는 낮은 임피던스 환경에서 더욱 큰 출력으로 초음파를 생성하며, 경계에서 발생된 임피던스 차이로 인한 저투과 문제를 페브리-페로 공진 현상을 통해 극복한다. 한편, 비파괴 검사를 수행하는 경우, 검사 정확도를 위해 짧은 주기의 신호가 선호된다는 점에서 입력 신호에 대한 메타물질의 민감도를 고려할 필요가 있다. 이에 대응하여 본 연구에서는 국부 영역의 임피던스를 증가 시킬 수 있는 메타물질 상판을 제안한다. 새롭게 정의된 전달행렬과 산란행렬을 이용하여 물리 현상을 규명하고 필요한 물리적 특성을 조사한다. 상판은 임피던스 차이를 발생시켜 초음파의 부분적 반사와 투과를 일으키는데, 페브리-페로 캐비티를 형성하는 기하 조건에서 임피던스 차이의 비율만 만큼 출력을 크게 향상시킨다. 또한, 상판 구조는 비공진 구조로 설계되어 상대적으로

낮은 입력 신호 민감도를 갖기 때문에 실용성이 매우 높다. 제안하는 탄성 메타물질은 높은 출력을 필요로 하는 초음파를 이용한 비파괴 검사 분야에 응용될 수 있을 것으로 기대한다.

주요어: 탄성 메타물질, 출력 향상, 전방향 전단 수평파, 유효 임피던스, 페브리-페롯 캐비티

학 번 : 2016-25899

ACKNOEWLEDGEMENTS

This research was supported by the National Research Foundation of Korea (NRF) Grant [CAMM-2014M3A6B3063711 and NRF-2022R1A2C2008067] contracted through the Institute of Advanced Machines and Design at Seoul National University funded by the Korea Ministry of Science, ICT & Future Planning